

Hybridization of topologically distinct quartet modes in three-terminal graphene Josephson junctions

Asmaul Smitha Rashid^{1,2}, Le Yi^{3,2}, Takashi Taniguchi⁴, Kenji Watanabe⁵,
Nitin Samarth^{3,6,2}, Régis Mélin⁷, Morteza Kayyalha^{1,2*}

¹Department of Electrical Engineering, The Pennsylvania State University, University Park, Pennsylvania 16802, USA.

²Materials Research Institute, The Pennsylvania State University, University Park, Pennsylvania 16802, USA.

³Department of Physics, The Pennsylvania State University, University Park, Pennsylvania 16802, USA.

⁴Research Center for Materials Nanoarchitectonics, National Institute for Materials Science, 1-1 Namiki, Tsukuba 305-0044, Japan.

⁵Research Center for Electronic and Optical Materials, National Institute for Materials Science, 1-1 Namiki, Tsukuba 305-0044, Japan.

⁶Department of Materials Science and Engineering, The Pennsylvania State University, University Park, Pennsylvania 16802, USA.

⁷Université Grenoble-Alpes, CNRS, Grenoble INP, Institut NEEL, Grenoble, France.

*Corresponding author. Email: mzr463@psu.edu

Multiterminal Josephson junctions offer a powerful playground for exploring exotic superconducting and topological phenomena beyond the reach of conventional two-terminal devices. In this work, we present the direct spectroscopic observation of Cooper quartet resonances, a signature of correlated tunneling of two Cooper pairs across the device, in a graphene three-terminal Josephson junction (3TJJ). Using tunneling spectroscopy, we visualize how Andreev bound states (ABS) evolve across a two-dimensional superconducting phase space, controlled by the two independent phase differences in the 3TJJ. These measurements reveal sharp local minima in the differential conductance spectra locked in a specific phase condition of superconducting phase variables. The resulting quantized trajectories around the compact torus of the superconducting phase variables reveal an underlying topological winding in the multipair transport. To interpret our results, we develop a theoretical model that connects the observed quartet resonances to the coherent hybridization of multiple ABS branches, a hallmark of the rich pairing process enabled by multiterminal geometries. Our results highlight the potential of multiterminal superconducting devices to host engineered superconducting states and pave the way for new approaches to topological band structure design based on phase-controlled, higher-order superconducting transport.

Introduction

Josephson junctions (JJs) underpin a wide range of superconducting quantum technologies (1–5), where coherent transport of Cooper pairs forms the basis for a multitude of device structures and basic physics studies, including Andreev level qubits (6–12), quantum sensors (13, 14), and topological phases (15). These studies focus on JJs with two superconducting terminals, where the Andreev bound state (ABS) energies depend on a single superconducting phase difference (16, 17).

Multiterminal Josephson junctions (MTJJs) expand this landscape by adding independent superconducting phase differences that control the energies of ABSs (18–22). These phase differences can be interpreted as quasi-momenta in a synthetic multi-dimensional crystal. The ABS spectra therefore resemble a band structure in higher dimensions, known as the Andreev band structure (17, 23–27). These band structures host unique properties such as higher-order Cooper multiplets (28), Andreev molecules (6, 21, 29, 30, 30–33), Floquet-ABS (34–37), nonequilibrium Andreev resonances (38, 39) and topological phases (17, 23–27, 40, 41), making MTJJs an unparalleled platform for studying exotic quantum states.

Among these emergent processes, Cooper multiplets such as quartets, in which two Cooper pairs coherently split across three terminals, stand out as a hallmark signature of multiterminal entanglement (28, 42–49). The quartet processes give rise to supercurrents that depend on novel combinations of phase variables (e.g., $\chi_q = 2\varphi_L - \varphi_R - \varphi_B$ or $\chi_q = \varphi_L - 2\varphi_R + \varphi_B$), where φ_i ($i = L, B, R$) denote the superconducting phases of the terminals S_L , S_B , and S_R , respectively and χ_q is the corresponding quartet phase variable. (Figure 1(a)). Theoretical work has proposed strategies to identify these multiplet states through current-voltage characteristics or supercurrent-phase measurements (28, 50, 51). Experimental evidence (42–45), though suggestive, remains largely indirect and often relies on integrated transport signatures that obscure the fine structure of the underlying ABS spectrum. Therefore, these approaches lack the resolution to resolve the structure of the underlying ABS associated with higher-order Cooper processes. A spectroscopic approach capable of isolating the ABS dispersions over multi-dimensional phase space is essential for unambiguous detection of Cooper quartets. Recent developments in tunneling spectroscopy of MTJJs (6, 30, 32, 33, 37, 52, 53) offer a powerful route to directly probe these multi-dimensional Andreev bands, providing insight into the details of their spectral features and topological properties (33, 53, 54). Yet, despite their potential, these studies have not been fully leveraged to explore the interplay of higher-order Cooper processes within the ABS spectrum.

In this work, we utilized a combined experimental and theoretical approach to probe the Andreev band structure and report quantized winding trajectories that indicate nontrivial topology in multipair processes. We determine how these winding sectors manifest and hybridize in the ABS spectrum. Our findings address whether and how these multipair processes are related to the emerging topological viewpoint in MTJJs. We specifically utilize superconducting tunneling spectroscopy in a three-terminal graphene JJ, accessing the full Andreev band structure as a function of the two independent superconducting phase differences. By fixing the tunnel probe bias and sweeping the two phases, we resolve the phase-dependent dispersion of ABSs. We observe spectroscopic signatures associated with the Cooper quartets, specifically, sharp resonances along specific phase combinations and quantized slope in the plane of the superconducting phase variables. Furthermore, we find avoided crossings for two quartet modes indicative of ABS

hybridization. This hybridization reveals the quantum mechanical nature of the quartets and shows that the topological winding structure alone is insufficient to describe the behavior of the Andreev bands. We compare our measurements to theoretical calculations that incorporate coherent tunneling processes in the MTJJ. The simulations qualitatively reproduce the key spectral features including quartet resonances supporting the overall quartet picture. Our results thus provide direct, phase-resolved spectroscopic evidence of higher-order Cooper quartet processes and establish graphene-based MTJJs as a versatile platform for exploring exotic quantum states in synthetic superconducting lattices.

Results

We fabricate three-terminal Josephson junctions on hBN/graphene/hBN van der Waals heterostructures, with edge-contacted superconducting terminals made of Ti (10 nm)/Al (80 nm). These terminals are coupled through the shared graphene region, allowing Josephson supercurrent to flow between them. The graphene channel is 0.6 μm wide, and each terminal is positioned approximately 0.6 μm from the center. Figure 1(b) shows a scanning electron microscope (SEM) image of a representative three-terminal junction. The three superconducting electrodes are labeled S_i ($i = L, B, R$). These terminals are connected to a common node D , forming two closed superconducting loops. Each terminal is characterized by its superconducting phase φ_i ($i = L, B, R$). The Josephson current in the 3TJJ is governed by Andreev bands, whose energies depend on the phase differences between the terminals. Assuming $\varphi_B = 0$, two independent phase differences, $\varphi_{L/R} = 2\pi\Phi_{L/R}/\Phi_0$, controlled by external magnetic fluxes $\Phi_{L/R}$, determine the behavior of the junction. These fluxes are applied via two Ti (10 nm)/Al (80 nm) bias lines for the left and right loops. Finally, a superconducting tunneling probe S_T is fabricated by edge-contacting graphene with Al (80 nm), without a Ti layer (53, 55–57). This probe enables tomography of the Andreev bands in the graphene-based 3TJJ.

Figure 1 (c) shows the measurement setup for Device 1, which is shown in Fig. 1 (b). The differential tunneling conductance is obtained as $G = dI_t/dV_t$ where the tunneling current (voltage) is measured between S_T and node D . In this device, if the voltage V_t on the tunneling tip is smaller than the superconducting gap Δ , then G is expected to have peaks that emerge in the tunneling current when the BCS gap-edge singularity in the density of states of the probe S_t matches the ABS energies (56–58). However, we still obtain a nontrivial signal if the bias voltage energy eV_t is larger than twice the gap. In this case, quasiparticles exchange between graphene and S_t will form a nonequilibrium Fermi surface at the chemical potential $\mu_N(V_t)$ (59–61). The tunnel probe in Device 1 exhibits a soft superconducting gap (see section I in the Supporting Information (SI) for more details). For tunneling voltages within the gap ($|eV_t| < \Delta$, with $\Delta \approx 180 \mu\text{eV}$), tunneling conductance directly measures the sub-gap Andreev bound states (ABSs). For voltages outside the gap ($|eV_t| > 2\Delta$), the probe accesses nonequilibrium ABSs via quasiparticle injection and relaxation in graphene, as described above.

Figure 1 (d) shows the tunneling conductance G as a function of independent phases φ_L and φ_R , tuned by fluxes Φ_L and Φ_R , at $V_t = 0$ V. We observe periodic modulation of G over φ_L and φ_R . The minima in the G map (referred to as resonances thereafter) follow a tilted plane along $\varphi_L = \varphi_R$ direction. These resonances are attributed to the presence of ABS between (S_L, S_B) and (S_R, S_B) whose energies disperse with the superconducting phases. Figures 2

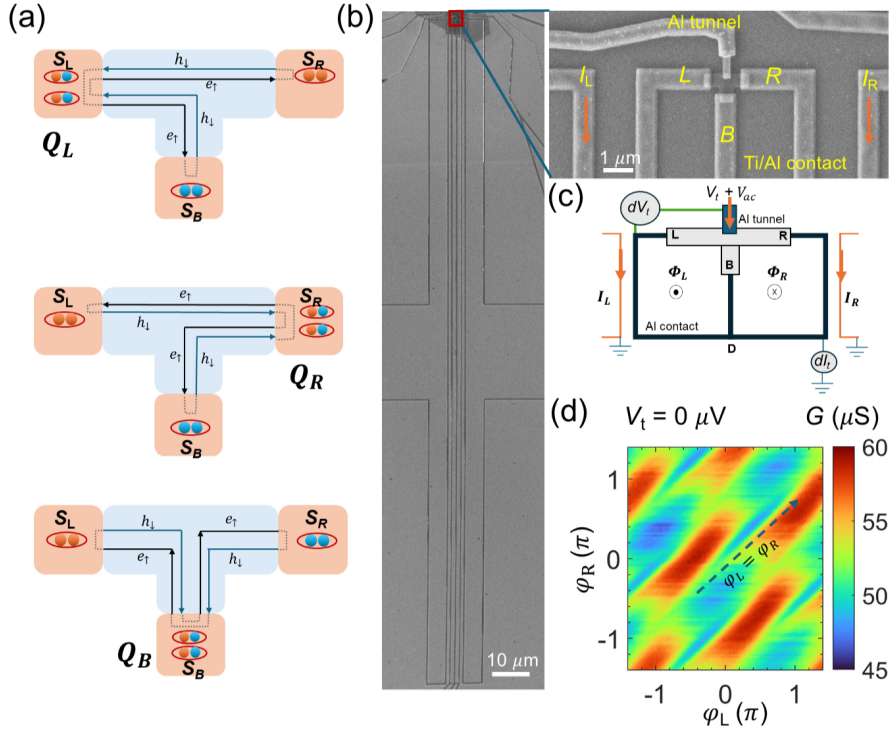


Figure 1: Schematics of Cooper quartet processes and experimental device. (a) Q_L , Q_R , and Q_B schematics represent three-terminal quartet processes where electron-hole conversion occurs twice at either S_L , S_R , or S_B , respectively. Q_L , Q_R , and Q_B have phase relations as $2\varphi_L - \varphi_R - \varphi_B$, $-\varphi_L + 2\varphi_R - \varphi_B$ and $-\varphi_L - \varphi_R + 2\varphi_B$, respectively. (b) Scanning electron microscope (SEM) image of a representative three-terminal JJ. The magnified SEM image on the right highlights the three superconducting terminals denoted as S_i ($i = L, B, R$). A fourth Al terminal is weakly coupled to the device forming a tunnel probe S_T . (c) Schematic representation of the device and the measurement setup. (d) Tunneling conductance G as a function of phases φ_L and φ_R at bias voltage $V_t = 0$ V. φ_L and φ_R are obtained by applying I_L and I_R to the flux bias lines with step sizes of $0.25 \mu\text{A}$ and $1 \mu\text{A}$, respectively.

(a-c) show the tunneling conductance G as a function of φ_L and φ_R at constant V_t 's. For $V_t < \Delta$, G exhibits periodic resonances corresponding to the presence of ABS between (S_L, S_B) and (S_R, S_B) . However, as V_t approaches Δ , the lines corresponding to the resonances [dominant minima in Figs. 2 (b-c)] realign along $\chi_q = 2\varphi_L - \varphi_R$ and $\chi_q = -\varphi_L + 2\varphi_R$. Furthermore, these two families of resonant minima (dark blue lines) create a diamond-like closed loop in φ_L, φ_R phase space as shown by the dashed lines in Fig. 2 (b). A recent study attributes such tilted resonant lines to an effect of the cross-talk between the left/right loops and the local magnetic field produced by the flux lines (33). However, we observe resonances of quantized slope 2 or $1/2$, controlled by the bias voltage. This bias-voltage evolution of the tilt cannot be explained by the crosstalk. As we discuss theoretically below, these observations point to a microscopic origin tied to higher-order Andreev processes.

To understand the underlying mechanisms behind our experimental observations, we theoretically calculate the Andreev resonances and their dependence on superconducting phase variables (see section III in the SI for details of

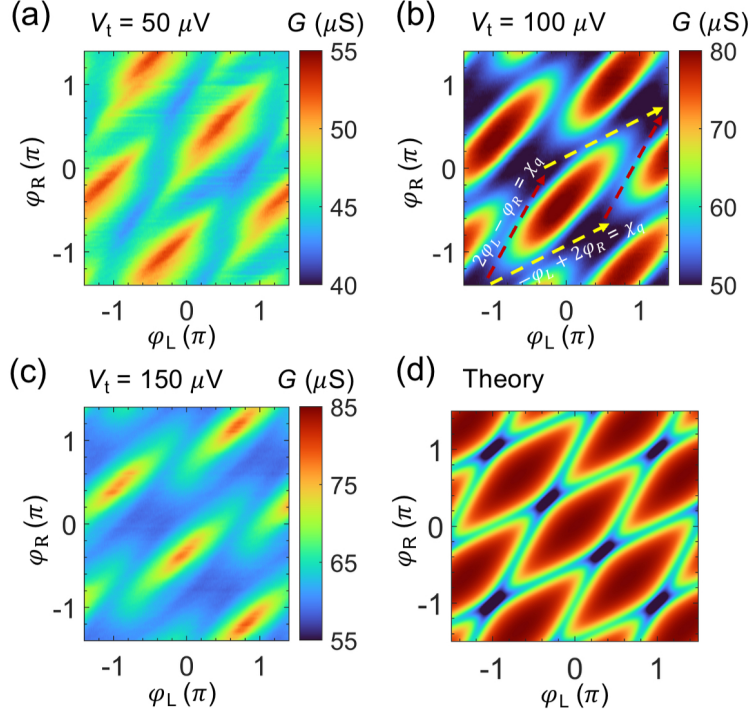


Figure 2: Tunneling spectroscopy in three-terminal JJ. (a-c) Tunneling conductance G as a function of independent phases φ_L and φ_R governed by fluxes Φ_L and Φ_R at various bias voltages $V_t = 50 \mu\text{V}$ (a), $V_t = 100 \mu\text{V}$ (b), and $V_t = 150 \mu\text{V}$ (c). The colormaps are obtained by varying I_L and I_R with a step sized of $0.25 \mu\text{A}$ and $1 \mu\text{A}$ respectively. (d) Theoretically calculated tunneling conductance as a function of phases φ_L and φ_R at dimensionless probe bias voltage $V_{t,eff} = |eV_t|/2\Delta$.

our theoretical calculations). We consider the proximity effect at a disordered normal-metal–insulator–superconductor (NIS) interface. At the NIS interface, a spin-up electron from the disordered metal (N) can be Andreev reflected as a spin-down hole while a Cooper pair is transmitted to S . However, due to the low contact transparency, a spin-up electron is highly likely to undergo normal reflection back into N and subsequently return to the interface because of the localizing effect of disorder. This process, involving multiple scattering events in the presence of disorder, can iterate until a Cooper pair is transmitted to S , and a hole is back-scattered to the normal region (2). To describe the analogous proximity-induced quartet mechanism in graphene-based MJJs, we employ a simple Random Phase Approximation (RPA) in which an elementary kernel is iterated (see Eq. 9 in the SI). Considering the two-dimensional nature ($D = 2$) of graphene, we find that constructive interference of the proximity effect emerges at fixed values of the superconducting phase difference for the two-terminal Josephson configuration, and at fixed values of the quartet phase in the three-terminal case.

Within this framework, a Cooper quartet resonance occurs when the total phase accumulated through the transmission of two pairs into S_L via S_R , S_B and S_R via S_L , S_B , becomes constructive (see Fig. S6). The quartet phases correspond to the sum of four Andreev reflection phase shifts at the SN interfaces, i.e., $\chi_q = 2\varphi_L - \varphi_R - \varphi_B$,

$-\varphi_L + 2\varphi_R - \varphi_B$, and $-\varphi_L - \varphi_R + 2\varphi_B$. We calculate the nonlocal Andreev reflection using Green's function formalism, where each reflection contributes a phase shift of $\pi/2$. From the constructive-interference condition in 2D, we obtain the spectrum of Cooper-quartet resonances and the associated energies (see Eq. 34 in the SI).

The theoretically calculated energy-phase relation of quartet resonances is consistent with our measurements, where we observe resonance lines along χ_q in the G map as shown in Fig. 2. However, the bias voltage V_t acts as an energy filter that controls transmission through different conduction channels. Energies near the gap edge correspond to channels with low transmission, while energies toward the middle of the gap correspond to more transparent, highly transmitting channels. Low transmission favors the two-terminal DC Josephson effect, whereas higher-order Andreev processes emerge at higher transmission. This explains why the DC Josephson effect appears near the gap edge, while quartet resonances occur near mid-gap. These findings are in agreement with our experimental observation of quartet resonance around $V_t \approx \Delta/1.8$ ($\approx 100 \mu\text{V}$).

We investigate the ABS resonances in the regime where $V_t \geq 2\Delta$ (see Figs. S2). In this regime, the ABS energies coincide with the nonequilibrium Fermi surface at the energy μ_N induced in the graphene region. The energy μ_N , approximated by $\mu_N^* \sim \sqrt{(eV_t)^2 - (2\Delta)^2}$, can be substantially lower than the applied voltage V_t to the superconducting probe S_T . Consequently, even in high bias regime $V_t \geq 2\Delta$, the effective Fermi energy $\mu_N \leq \Delta$ remains smaller than the gap, allowing spectroscopy of in-gap states (see Fig. S7). As a result, we observe the characteristic signature of the quartet resonant family that reappears at $V_t \approx 2.78\Delta$ ($\approx 500 \mu\text{V}$) (see Fig. S2(d)), consistent with the features previously identified in Fig. 2(b). Taken together, these observations demonstrate the robustness of quartet resonances against large bias voltages and highlight the versatility of our device for engineering high-order correlated processes.

Figure 2(d) shows the theoretically calculated tunneling conductance map in the (φ_L, φ_R) plane. The phenomenological model incorporates the two possible quartet configurations and calculates the conductance. The conductance map $g_0(\varphi_L, \varphi_R, V_{t,\text{eff}})$ is then computed on a discrete grid of phase values to produce the intersecting quartet resonance lines which qualitatively reproduces the key features of the quartet resonances observed experimentally. The details of the calculation is provided in section VI of the SI.

Figure. 3(a) shows the differential conductance G as a function of φ_L and φ_R at the bias voltage $V_t = 100 \mu\text{V}$. The white dashed lines indicate the two quartet-resonance branches forming a diamond like pattern. To experimentally track the behavior of these two branches, we extract diagonal line cuts from Fig. 3(a) along $\varphi_L = t$ and $\varphi_R = -t + \alpha$. Figure 3(b) plots line cuts of G as a function of the variable t for $\alpha = 0$ (blue) and $\alpha = \pi/3$ (orange). We can obtain line cuts similar to Fig. 3(b) by varying α (π) between -1 to 1 with a step size of 1/100. For each trace (using a Gaussian smoothing), we identify the local minima in G and record the corresponding phases $\varphi_L(n)$ at the values of α . These points are plotted in Fig. 3(c), yielding a series of continuous curves that track quartet branches as α is varied. Notably, these curves exhibit robust continuity and show avoided crossing between the branches, indicating hybridization of quartet modes.

Figure 3(d) shows theoretically calculated two quartet-resonance branches with quartet phase variables $\chi_q = 2\varphi_L - \varphi_R$ and $\chi_q = -\varphi_L + 2\varphi_R$ indicating slope 2 (red) and slope 1/2 (blue), respectively. We see that the resonant interaction of Cooper quartets in Fig. 3(c) contrasts with the assumption of independent quartet spectra that underlies

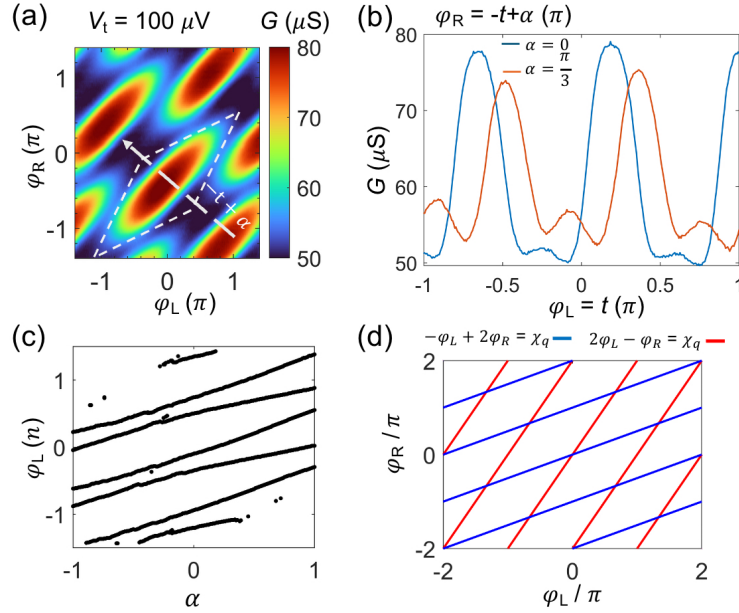


Figure 3: Hybridization of quartet modes. (a) Tunneling conductance G as a function of independent phases φ_L and φ_R at the bias voltage $V_t = 100 \mu\text{V}$. The colormap is obtained by varying I_L and I_R with a step sized of $0.25 \mu\text{A}$ and $1 \mu\text{A}$, respectively. White dashed lines (diamond shape) indicate two modes of the quartet resonance with quartet phase variables $\chi_q = 2\varphi_L - \varphi_R$ and $\chi_q = -\varphi_L + 2\varphi_R$. (b) Diagonal line cuts along $\varphi_L = t$ and $\varphi_R = -t + \alpha$ with the variable $\varphi_L = t$ plotted on the x-axis and the tunneling conductance G on the y-axis for $\alpha = 0$ (blue) and $\alpha = \pi/3$ (orange). Local minima of G can be obtained at each value of α . (c) The scatter plot shows $\varphi_L (n)$ as a function of α . The minima of G and the corresponding phases $\varphi_L (n)$ is obtained by varying $\alpha (\pi)$ (between -1 to 1) with a step size of $1/100$. (d) Illustration of two families of Cooper quartet resonances with quartet phase variables $\chi_q = 2\varphi_L - \varphi_R$ and $\chi_q = -\varphi_L + 2\varphi_R$ indicating slope 2 (red) and slope $1/2$ (blue), respectively.

the theoretical calculations. In contrast to experiment, the calculated quartet spectra show direct crossings between two quartet branches. At these crossings, bistability emerges between distinct quartet states. In one- and three-dimensional systems, such intersections would normally lead to level repulsion, causing the DC quartet current (proportional to $\delta E/\delta\varphi$) to vanish at the avoided crossing. However, in large-scale two-dimensional systems the quartet spectrum forms a continuum at fixed superconducting phases. But we argue that, if the two quartet branches crossed without hybridization, the coexistence of degenerate states would generate partition noise in the DC quartet supercurrent, which contradicts the well-established result that Josephson currents between BCS superconductors are noiseless at zero temperature (62). This apparent contradiction is resolved by recognizing that the quartet current must vanish at the crossing points of the two branches. The theoretical Fig. 3(d) is deduced from a multiterminal generalization of long highly transparent two-terminal Josephson junctions (2), where the ABS energies are free to cross at the phase differences of 0 and π . Including the realistic backscattering produces avoided crossings in the two-terminal ABS spectra, and hybridization between the ABS branches (4). Thus, theory predicts a vanishing quartet current at the

crossing points, consistent with the avoided crossings (hybridization) observed in the experimental G maps.

Although our analysis focuses on the microscopic origin of Cooper quartets, the structure of the resonances naturally invites a broader topological interpretation. Because the superconducting phase is defined modulo 2π , the control parameters (φ_L, φ_R) form a compact two-dimensional torus that acts as a synthetic Brillouin zone for the Andreev spectrum. The two observed distinct branches of quartet resonances follow the relations $2\varphi_L - \varphi_R = \text{const.}$ and $-\varphi_L + 2\varphi_R = \text{const.}$ These relations correspond to straight, quantized winding trajectories on this toroidal phase space. These winding conditions of the quartets echo classical topological classifications of closed trajectories, analogous to early knot theory (63). In multiterminal Josephson junctions, integer combinations of superconducting phases play a similar role and may be used to organize higher-order Cooper multiplets such as quartets, sextets, and beyond.

Our experiment demonstrates a key departure from this classical picture. At the intersection of the two winding families, the resonances do not cross freely, as would be expected from topologically distinct classical trajectories. Instead, we observe clear avoided crossings. This behavior reflects coherent hybridization between Andreev bound states belonging to different winding sectors and shows that the Andreev spectrum cannot be understood by classical winding arguments alone. The avoided crossings therefore serve as direct signatures of the quantum nature of the Andreev bands on the torus of the superconducting phase variables. The winding conditions determine where the resonances appear, while quantum coherence controls how these resonances interact. Classical winding topology alone cannot account for this hybridization, its resolution requires the full quantum mechanical structure of the Andreev spectrum.

Taken together, these results suggest that multiterminal Josephson junctions naturally host two distinct forms of topology. One is classical, defined by integer phase-winding sectors that classify multiplet processes. The other is quantum, encoded in the Andreev band structure on the phase torus, which can in principle carry Berry curvature (64), Chern number (17), or isolated singularities in higher dimensional phase spaces. The observed hybridization of quartet modes demonstrates that these two distinct forms of topology can interact. Extending this spectroscopic approach to four-terminal junctions, where the phase space becomes three dimensional, offers a promising route to explore whether these two topological structures remain separate or combine to produce new forms of topology unique to superconducting circuits with phase control.

Conclusion

In summary, we have performed a tomographic study of Andreev bound states in a graphene-based three-terminal Josephson junction using phase-resolved tunneling spectroscopy. Independent control of the left and right phases through a double-SQUID geometry enabled direct mapping of the synthetic Andreev band structure. By tuning the bias voltage V_t , we accessed higher-order Andreev processes and identified resonances that satisfy the quartet phase relations. Because the phase space forms a compact torus, these resonances trace quantized winding trajectories associated with distinct quartet modes. At the intersections of these trajectories, we observe avoided crossings, signaling coherent

hybridization between modes belonging to different winding sectors. A microscopic model reproduces the phase structure and explains the avoided crossings.

When $V_t > 2\Delta/e$, we showed that quartet patterns re-emerge, owing to relaxation of injected quasiparticles toward an effective nonequilibrium chemical potential. By establishing a direct, phase-resolved link between tunable multiterminal geometries and high-order Cooper-pair transport, our results provide a quantitative benchmark for the detection of Cooper quartets and demonstrate a practical path toward engineering synthetic Andreev band structures with non-trivial topology. This spectroscopic approach can now be extended to four-terminal junctions, where higher-order Cooper multiplets (sextets) (65), Weyl, and additional topological phases are predicted (41,66). Graphene multiterminal junctions therefore emerge as a powerful and versatile platform for manipulating correlated superconducting states, and for realizing quantum phase design in higher-dimensional Andreev crystals.

Materials and Methods

Device Fabrication

Graphene and hexagonal boron nitride (hBN) flakes were mechanically exfoliated using adhesive tape. The heterostructures were assembled using a standard dry-transfer technique, in which graphene was encapsulated between hBN layers with a hBN thickness of approximately 35 nm each. The device channel was defined by electron-beam lithography followed by reactive ion etching using a CHF_3/O_2 plasma. Electrical contacts were fabricated by electron-beam evaporation onto freshly etched graphene edges. Ti (10 nm)/Al (80 nm) were deposited to form edge contacts and flux lines. A superconducting tunnel probe, consisting of an 80 nm Al layer without an adhesion layer, was deposited using BN– TiB_2 crucibles at a rate of 0.4 \AA s^{-1} . During deposition, the chamber pressure was maintained at 1×10^{-7} mtorr.

Electrical Transport

All the electrical transport measurements were performed inside a Bluefors LD250 dilution fridge, equipped with QDevil filtered DC lines. A dc bias voltage V_t was applied to the tunnel probe with a small signal ac voltage $V_{\text{ac}} \approx 5 \mu\text{V}$, and the tunneling voltage (dV_t) was measured between S_T and node D using a lock-in amplifier. Another lock-in amplifier was used to measure the tunneling current (dI_t). The tunneling current dI_t was amplified via a current to voltage preamplifier whose voltage was subsequently measured using another lock-in amplifier. The resulted differential tunneling conductance is obtained as $G = dI_t/dV_t$.

Acknowledgements

Funding

M.K. and A.S.R. acknowledge funding from the the US National Science Foundation under award DMR 2415756. Device fabrication was supported through the Pennsylvania State University Materials Research Science and Engineering

Center supported by the US National Science Foundation (DMR 2011839). R.M. acknowledges the financial support from the SUPRADEVMAT International Project between the French CNRS-Grenoble and the German KIT-Karlsruhe.

Data Availability

All data supporting the conclusions in the paper are present in the paper and/or the Supplementary Materials.

References

1. A. Furusaki, M. Tsukada, Current-carrying states in Josephson junctions. *Phys. Rev. B* **43**, 10164–10169 (1991), doi:10.1103/PhysRevB.43.10164, <https://link.aps.org/doi/10.1103/PhysRevB.43.10164>.
2. I. O. Kulik, Macroscopic Quantization and the Proximity Effect in S-N-S Junctions. *Soviet Journal of Experimental and Theoretical Physics* **30**, 944 (1969).
3. C. Ishii, Josephson Currents through Junctions with Normal Metal Barriers. *Progress of Theoretical Physics* **44** (6), 1525–1547 (1970), doi:10.1143/PTP.44.1525, <https://doi.org/10.1143/PTP.44.1525>.
4. P. F. Bagwell, Suppression of the Josephson current through a narrow, mesoscopic, semiconductor channel by a single impurity. *Phys. Rev. B* **46**, 12573–12586 (1992), doi:10.1103/PhysRevB.46.12573, <https://link.aps.org/doi/10.1103/PhysRevB.46.12573>.
5. R. Kraft, *et al.*, Tailoring supercurrent confinement in graphene bilayer weak links. *Nature Communications* **9** (1), 1722 (2018), doi:10.1038/s41467-018-04153-4, <https://doi.org/10.1038/s41467-018-04153-4>.
6. M. Coraiola, *et al.*, Spin-degeneracy breaking and parity transitions in three-terminal Josephson junctions (2023).
7. N. M. Chtchelkatchev, Y. V. Nazarov, Andreev Quantum Dots for Spin Manipulation. *Phys. Rev. Lett.* **90**, 226806 (2003), doi:10.1103/PhysRevLett.90.226806, <https://link.aps.org/doi/10.1103/PhysRevLett.90.226806>.
8. A. Zazunov, V. S. Shumeiko, E. N. Bratus', J. Lantz, G. Wendin, Andreev Level Qubit. *Phys. Rev. Lett.* **90**, 087003 (2003), doi:10.1103/PhysRevLett.90.087003, <https://link.aps.org/doi/10.1103/PhysRevLett.90.087003>.
9. C. Padurariu, Y. V. Nazarov, Theoretical proposal for superconducting spin qubits. *Phys. Rev. B* **81**, 144519 (2010), doi:10.1103/PhysRevB.81.144519, <https://link.aps.org/doi/10.1103/PhysRevB.81.144519>.
10. M. Hays, *et al.*, Coherent manipulation of an Andreev spin qubit. *Science* **373** (6553), 430–433 (2021), doi:10.1126/science.abf0345, <https://www.science.org/doi/abs/10.1126/science.abf0345>.
11. M. Pita-Vidal, *et al.*, Direct manipulation of a superconducting spin qubit strongly coupled to a transmon qubit. *Nature Physics* **19** (8), 1110–1115 (2023), doi:10.1038/s41567-023-02071-x, <https://doi.org/10.1038/s41567-023-02071-x>.
12. E. C. Gingrich, *et al.*, Controllable $0-\pi$ Josephson junctions containing a ferromagnetic spin valve. *Nature Physics* **12** (6), 564–567 (2016), doi:10.1038/nphys3681, <https://doi.org/10.1038/nphys3681>.
13. Y. Chen, Y. V. Nazarov, Spintronics with a Weyl point in superconducting nanostructures. *Phys. Rev. B* **103**, 165424 (2021), doi:10.1103/PhysRevB.103.165424, <https://link.aps.org/doi/10.1103/PhysRevB.103.165424>.

14. G.-H. Lee, *et al.*, Graphene-based Josephson junction microwave bolometer. *Nature* **586** (7827), 42–46 (2020), doi:10.1038/s41586-020-2752-4, <https://doi.org/10.1038/s41586-020-2752-4>.
15. X.-L. Qi, S.-C. Zhang, Topological insulators and superconductors. *Rev. Mod. Phys.* **83**, 1057–1110 (2011), doi:10.1103/RevModPhys.83.1057, <https://link.aps.org/doi/10.1103/RevModPhys.83.1057>.
16. J. A. Sauls, Andreev bound states and their signatures. *Philosophical Transactions of the Royal Society A: Mathematical, Physical and Engineering Sciences* **376** (2125), 20180140 (2018), doi:10.1098/rsta.2018.0140, <https://royalsocietypublishing.org/doi/abs/10.1098/rsta.2018.0140>.
17. E. V. Repin, Y. Chen, Y. V. Nazarov, Topological properties of multiterminal superconducting nanostructures: Effect of a continuous spectrum. *Phys. Rev. B* **99**, 165414 (2019), doi:10.1103/PhysRevB.99.165414, <https://link.aps.org/doi/10.1103/PhysRevB.99.165414>.
18. N. Pankratova, *et al.*, Multiterminal Josephson Effect. *Phys. Rev. X* **10**, 031051 (2020), doi:10.1103/PhysRevX.10.031051, <https://link.aps.org/doi/10.1103/PhysRevX.10.031051>.
19. G. V. Graziano, J. S. Lee, M. Pendharkar, C. J. Palmstrøm, V. S. Pribiag, Transport studies in a gate-tunable three-terminal Josephson junction. *Phys. Rev. B* **101**, 054510 (2020), doi:10.1103/PhysRevB.101.054510, <https://link.aps.org/doi/10.1103/PhysRevB.101.054510>.
20. A. W. Draelos, *et al.*, Supercurrent Flow in Multiterminal Graphene Josephson Junctions. *Nano Letters* **19** (2), 1039–1043 (2019), doi:10.1021/acs.nanolett.8b04330, <https://doi.org/10.1021/acs.nanolett.8b04330>.
21. E. G. Arnault, *et al.*, Multiterminal Inverse AC Josephson Effect. *Nano Letters* **21** (22), 9668–9674 (2021), pMID: 34779633, doi:10.1021/acs.nanolett.1c03474, <https://doi.org/10.1021/acs.nanolett.1c03474>.
22. F. J. Matute-Cañadas, L. Tosi, A. L. Yeyati, Quantum circuits with multiterminal Josephson-Andreev junctions (2023).
23. R.-P. Riwar, M. Houzet, J. S. Meyer, Y. V. Nazarov, Multi-terminal Josephson junctions as topological matter. *Nature Communications* **7** (1), 11167 (2016), doi:10.1038/ncomms11167, <https://doi.org/10.1038/ncomms11167>.
24. J. S. Meyer, M. Houzet, Nontrivial Chern Numbers in Three-Terminal Josephson Junctions. *Phys. Rev. Lett.* **119**, 136807 (2017), doi:10.1103/PhysRevLett.119.136807, <https://link.aps.org/doi/10.1103/PhysRevLett.119.136807>.
25. L. Peralta Gavensky, G. Usaj, C. A. Balseiro, Topological phase diagram of a three-terminal Josephson junction: From the conventional to the Majorana regime. *Phys. Rev. B* **100**, 014514 (2019), doi:10.1103/PhysRevB.100.014514, <https://link.aps.org/doi/10.1103/PhysRevB.100.014514>.
26. V. Chandrasekhar, Probing the topological band structure of diffusive multiterminal Josephson junction devices with conductance measurements. *Applied Physics Letters* **121** (22), 222601 (2022), doi:10.1063/5.0125708, <https://doi.org/10.1063/5.0125708>.

27. L. P. Gavensky, G. Usaj, C. A. Balseiro, Multi-terminal Josephson junctions: A road to topological flux networks. *Europhysics Letters* **141** (3), 36001 (2023), doi:10.1209/0295-5075/acb2f6, <https://dx.doi.org/10.1209/0295-5075/acb2f6>.

28. D. C. Ohnmacht, *et al.*, Quartet tomography in multiterminal Josephson junctions. *Phys. Rev. B* **109**, L241407 (2024), doi:10.1103/PhysRevB.109.L241407, <https://link.aps.org/doi/10.1103/PhysRevB.109.L241407>.

29. V. Kornich, H. S. Barakov, Y. V. Nazarov, Fine energy splitting of overlapping Andreev bound states in multiterminal superconducting nanostructures. *Phys. Rev. Res.* **1**, 033004 (2019), doi:10.1103/PhysRevResearch.1.033004, <https://link.aps.org/doi/10.1103/PhysRevResearch.1.033004>.

30. S. Matsuo, *et al.*, Phase-dependent Andreev molecules and superconducting gap closing in coherently-coupled Josephson junctions. *Nature Communications* **14** (1), 8271 (2023), doi:10.1038/s41467-023-44111-3, <https://doi.org/10.1038/s41467-023-44111-3>.

31. M. Kocsis, Z. Scherübl, G. Fülöp, P. Makk, S. Csonka, Strong nonlocal tuning of the current-phase relation of a quantum dot based Andreev molecule (2024), <https://arxiv.org/abs/2303.14842>.

32. J. Pillet, V. Benzoni, J. Griesmar, J.-L. Smirr, C. O. Girit, Nonlocal Josephson Effect in Andreev Molecules. *Nano Letters* **19** (10), 7138–7143 (2019), doi:10.1021/acs.nanolett.9b02686, <https://doi.org/10.1021/acs.nanolett.9b02686>.

33. M. Coraiola, *et al.*, Phase-engineering the Andreev band structure of a three-terminal Josephson junction. *Nature Communications* **14** (1), 6784 (2023), doi:10.1038/s41467-023-42356-6, <https://doi.org/10.1038/s41467-023-42356-6>.

34. T. Oka, S. Kitamura, Floquet Engineering of Quantum Materials. *Annual Review of Condensed Matter Physics* **10** (Volume 10, 2019), 387–408 (2019), doi:<https://doi.org/10.1146/annurev-conmatphys-031218-013423>, <https://www.annualreviews.org/content/journals/10.1146/annurev-conmatphys-031218-013423>.

35. D. T. Liu, J. Shabani, A. Mitra, Floquet Majorana zero and π modes in planar Josephson junctions. *Phys. Rev. B* **99**, 094303 (2019), doi:10.1103/PhysRevB.99.094303, <https://link.aps.org/doi/10.1103/PhysRevB.99.094303>.

36. S. Park, *et al.*, Steady Floquet–Andreev states in graphene Josephson junctions. *Nature* **603** (7901), 421–426 (2022), doi:10.1038/s41586-021-04364-8, <https://doi.org/10.1038/s41586-021-04364-8>.

37. D. J. Carrad, *et al.*, Photon-Assisted Tunneling of High-Order Multiple Andreev Reflections in Epitaxial Nanowire Josephson Junctions. *Nano Letters* **22** (15), 6262–6267 (2022), pMID: 35862144, doi:10.1021/acs.nanolett.2c01840, <https://doi.org/10.1021/acs.nanolett.2c01840>.

38. A. S. Rashid, *et al.*, Nonequilibrium Andreev resonances in ballistic graphene Andreev interferometers. *Phys. Rev. B* **111**, L180504 (2025), doi:10.1103/PhysRevB.111.L180504, <https://link.aps.org/doi/10.1103/PhysRevB.111.L180504>.

39. R. Mélin, A. S. Rashid, M. Kayyalha, Ballistic Andreev interferometers. *Phys. Rev. B* **110**, 235419 (2024), doi:10.1103/PhysRevB.110.235419, <https://link.aps.org/doi/10.1103/PhysRevB.110.235419>.

40. E. Strambini, *et al.*, The ω -SQUIPT as a tool to phase-engineer Josephson topological materials. *Nature Nanotechnology* **11** (12), 1055–1059 (2016), <https://www.nature.com/articles/nnano.2016.157>.

41. H.-Y. Xie, M. G. Vavilov, A. Levchenko, Weyl nodes in Andreev spectra of multiterminal Josephson junctions: Chern numbers, conductances, and supercurrents. *Physical Review B* **97** (3), 035443 (2018).

42. M. Gupta, *et al.*, Evidence for π -shifted Cooper quartets and few-mode transport in PbTe nanowire three-terminal Josephson junctions (2024).

43. G. V. Graziano, *et al.*, Selective control of conductance modes in multi-terminal Josephson junctions. *Nature Communications* **13** (2022), doi:10.1038/s41467-022-33682-2, <https://doi.org/10.1038/s41467-022-33682-2>.

44. F. Zhang, *et al.*, Andreev processes in mesoscopic multiterminal graphene Josephson junctions. *Phys. Rev. B* **107**, L140503 (2023), doi:10.1103/PhysRevB.107.L140503, <https://link.aps.org/doi/10.1103/PhysRevB.107.L140503>.

45. Y. Cohen, *et al.*, Nonlocal supercurrent of quartets in a three-terminal Josephson junction. *Proceedings of the National Academy of Sciences* **115** (27), 6991–6994 (2018), <https://www.pnas.org/doi/10.1073/pnas.1800044115>.

46. K.-F. Huang, *et al.*, Evidence for 4 e charge of Cooper quartets in a biased multi-terminal graphene-based Josephson junction. *Nature communications* **13** (1), 3032 (2022).

47. R. Mélin, *et al.*, D.C. Josephson transport by quartets and other Andreev resonances in superconducting bijunctions. *Journal of Physics: Conference Series* **568** (5), 052006 (2014), doi:10.1088/1742-6596/568/5/052006.

48. A. H. Pfeffer, *et al.*, Subgap structure in the conductance of a three-terminal Josephson junction. *Physical Review B* **90** (7), 075401 (2014).

49. A. Freyn, B. Douçot, D. Feinberg, R. Mélin, Production of Nonlocal Quartets and Phase-Sensitive Entanglement in a Superconducting Beam Splitter. *Phys. Rev. Lett.* **106**, 257005 (2011), doi:10.1103/PhysRevLett.106.257005, <https://link.aps.org/doi/10.1103/PhysRevLett.106.257005>.

50. R. Mélin, M. Sotto, D. Feinberg, J.-G. Caputo, B. Douçot, Gate-tunable zero-frequency current cross correlations of the quartet state in a voltage-biased three-terminal Josephson junction. *Physical Review B* **93** (11), 115436 (2016).

51. J. Rech, *et al.*, Proposal for the observation of nonlocal multipair production. *Phys. Rev. B* **90**, 075419 (2014), doi:10.1103/PhysRevB.90.075419, <https://link.aps.org/doi/10.1103/PhysRevB.90.075419>.

52. S. Matsuo, *et al.*, Phase engineering of anomalous Josephson effect derived from Andreev molecules. *Science Advances* **9** (50), eadj3698 (2023), doi:10.1126/sciadv.adj3698, <https://www.science.org/doi/abs/10.1126/sciadv.adj3698>.

53. W. Jung, *et al.*, Tunneling spectroscopy of Andreev bands in multiterminal graphene-based Josephson junctions. *Science Advances* **11** (21), eads0342 (2025), doi:10.1126/sciadv.ads0342, <https://www.science.org/doi/abs/10.1126/sciadv.ads0342>.

54. T. Antonelli, *et al.*, Exploring the energy spectrum of a four-terminal Josephson junction: Towards topological Andreev band structures (2025), <https://arxiv.org/abs/2501.07982>.

55. L. Bretheau, *et al.*, Tunnelling spectroscopy of Andreev states in graphene. *Nature Physics* **13** (8), 756–760 (2017), doi:10.1038/nphys4110, <https://doi.org/10.1038/nphys4110>.

56. D. McCumber, Tunneling and Weak-Link Superconductor Phenomena Having Potential Device Applications. *Journal of Applied Physics* **39** (6), 2503–2508 (1968).

57. I. Giaever, Energy Gap in Superconductors Measured by Electron Tunneling. *Phys. Rev. Lett.* **5**, 147–148 (1960), doi:10.1103/PhysRevLett.5.147, <https://link.aps.org/doi/10.1103/PhysRevLett.5.147>.

58. G. Falci, D. Feinberg, F. W. J. Hekking, Correlated tunneling into a superconductor in a multiprobe hybrid structure. *Europhysics Letters* **54** (2), 255 (2001), doi:10.1209/epl/i2001-00303-0, <https://doi.org/10.1209/epl/i2001-00303-0>.

59. S.-K. Yip, Energy-resolved supercurrent between two superconductors. *Phys. Rev. B* **58**, 5803–5807 (1998), doi:10.1103/PhysRevB.58.5803, <https://link.aps.org/doi/10.1103/PhysRevB.58.5803>.

60. A. Kadigrobov, A. Zagoskin, R. I. Shekhter, M. Jonson, Giant conductance oscillations controlled by supercurrent flow through a ballistic mesoscopic conductor. *Phys. Rev. B* **52**, R8662–R8665 (1995), doi:10.1103/PhysRevB.52.R8662, <https://link.aps.org/doi/10.1103/PhysRevB.52.R8662>.

61. R. Mélin, A. S. Rashid, R. Danneau, M. Kayyalha, Revisiting the adiabatic limit in ballistic multiterminal Josephson junctions (2025), <https://arxiv.org/abs/2508.17367>.

62. R. Mélin, M. Sotto, D. Feinberg, J.-G. Caputo, B. Douçot, Gate-tunable zero-frequency current cross correlations of the quartet state in a voltage-biased three-terminal Josephson junction. *Phys. Rev. B* **93**, 115436 (2016), doi:10.1103/PhysRevB.93.115436, <https://link.aps.org/doi/10.1103/PhysRevB.93.115436>.

63. W. Haken, Über das Homöomorphieproblem der 3-Mannigfaltigkeiten. I. *Mathematische Zeitschrift* **80**, 89–120 (1962/63), <http://eudml.org/doc/170089>.

64. L. Peralta Gavensky, G. Usaj, D. Feinberg, C. A. Balseiro, Berry curvature tomography and realization of topological Haldane model in driven three-terminal Josephson junctions. *Phys. Rev. B* **97**, 220505 (2018), doi: 10.1103/PhysRevB.97.220505, <https://link.aps.org/doi/10.1103/PhysRevB.97.220505>.

65. M. R. Ebert, D. C. Ohnmacht, W. Belzig, J. C. Cuevas, Sextets in four-terminal Josephson junctions (2025), <https://arxiv.org/abs/2507.23464>.

66. A. Burkov, L. Balents, Weyl semimetal in a topological insulator multilayer. *Physical review letters* **107** (12), 127205 (2011).

67. H. Meier, V. I. Fal'ko, L. Glazman, Edge effects in the magnetic interference pattern of a ballistic SNS junction. *Physical Review B* **93**, 184506 (2016).

68. T. Meng, S. Florens, P. Simon, Self-consistent description of Andreev bound states in Josephson quantum dot devices. *Physical Review B* **79**, 224521 (2009).

69. R. Mélin, Ultralong-distance quantum correlations in three-terminal Josephson junctions. *Physical Review B* **104**, 075402 (2021).

70. R. L. Klees, G. Rastelli, J. C. Cuevas, W. Belzig, Microwave Spectroscopy Reveals the Quantum Geometric Tensor of Topological Josephson Matter. *Physical Review Letters* **124**, 197002 (2020).

71. R. Mélin, C. B. Winkelmann, R. Danneau, Magnetointerferometry of multiterminal Josephson junctions. *Physical Review B* **109**, 125406 (2024).

72. F. W. J. Hekking, Y. V. Nazarov, Interference of two electrons entering a superconductor. *Physical Review Letters* **71**, 1625 (1993).

73. F. W. J. Hekking, Y. V. Nazarov, Subgap conductivity of a superconductor–normal-metal tunnel interface. *Physical Review B* **49**, 6847 (1994).

74. J. A. Melsen, C. W. J. Beenakker, Reflectionless tunneling through a double-barrier NS junction. *Physica B* **203**, 219 (1994).

75. G. Blonder, M. Tinkham, T. Klapwijk, Transition from metallic to tunneling regimes in superconducting microconstrictions: Excess current, charge imbalance, and supercurrent conversion. *Physical Review B* **25** (7), 4515 (1982).

76. C. Caroli, R. Combescot, P. Nozieres, D. Saint-James, Direct calculation of the tunneling current. *Journal of Physics C: Solid State Physics* **4** (8), 916 (1971), doi:10.1088/0022-3719/4/8/018, <https://dx.doi.org/10.1088/0022-3719/4/8/018>.

77. C. Caroli, R. Combescot, P. Nozieres, D. Saint-James, A direct calculation of the tunnelling current: IV. Electron-phonon interaction effects. *Journal of Physics C: Solid State Physics* **5** (1), 21 (1972), doi:10.1088/0022-3719/5/1/006, <https://dx.doi.org/10.1088/0022-3719/5/1/006>.

78. J. C. Cuevas, A. Martín-Rodero, A. Levy Yeyati, Hamiltonian approach to the transport properties of superconducting quantum point contacts. *Physical Review B* **54**, 7366 (1996).

79. R. Mélin, A. S. Rashid, R. Danneau, M. Kayyalha, Revisiting the adiabatic limit in ballistic multiterminal Josephson junctions. *arXiv* (2025).

80. H. Nakano, H. Takayanagi, Quasiparticle interferometer controlled by quantum-correlated Andreev reflection. *Solid State Communications* **80**, 997 (1991).

81. A. V. Zaitsev, Effect of quasiparticle interference on the conductance of mesoscopic superconductor-normal-metal coupled systems. *Physics Letters A* **194**, 315 (1994).

82. A. Kadigrobov, A. Zagoskin, R. I. Shekhter, M. Jonson, Giant conductance oscillations controlled by supercurrent flow through a ballistic mesoscopic conductor. *Physical Review B* **52**, 8662 (1995).

83. A. F. Volkov, New phenomena in Josephson SINIS junctions. *Physical Review Letters* **74**, 4730 (1995).

84. T. H. Stoof, Y. V. Nazarov, Flux effect in superconducting hybrid Aharonov–Bohm rings. *Physical Review B* **54**, R772 (1996).

85. T. H. Stoof, Y. V. Nazarov, Kinetic-equation approach to diffusive superconducting hybrid devices. *Physical Review B* **53**, 14496 (1996).

86. F. K. Wilhelm, G. Schön, A. D. Zaikin, Mesoscopic Superconducting–Normal Metal–Superconducting Transistor. *Physical Review Letters* **81**, 1682 (1998).

87. S.-K. Yip, Energy-resolved supercurrent between two superconductors. *Physical Review B* **58**, 5803 (1998).

88. W. Belzig, F. K. Wilhelm, C. Bruder, G. Schön, A. D. Zaikin, Quasiclassical Green’s function approach to mesoscopic superconductivity. *Superlattices and Microstructures* **25**, 1251 (1999).

89. A. V. Galaktionov, A. D. Zaikin, L. S. Kuzmin, Andreev interferometer with three superconducting electrodes. *Physical Review B* **85**, 224523 (2012).

90. A. V. Galaktionov, A. D. Zaikin, Current-biased Andreev interferometer. *Physical Review B* **88**, 104513 (2013).

91. P. E. Dolgirev, M. S. Kalenkov, A. D. Zaikin, Interplay between Josephson and Aharonov–Bohm effects in Andreev interferometers. *Scientific Reports* **9**, 1301 (2019).

92. P. E. Dolgirev, M. S. Kalenkov, A. E. Tarkhov, A. D. Zaikin, Phase coherent electron transport in asymmetric cross-like Andreev interferometers. *Physical Review B* **100**, 054511 (2019).

93. G. Falci, D. Feinberg, F. W. J. Hekking, Correlated tunneling into a superconductor in a multiprobe hybrid structure. *Europhysics Letters* **54**, 255 (2001).

94. R. Mélin, D. Feinberg, Sign of the crossed conductances at a ferromagnet/superconductor/ferromagnet double interface. *Physical Review B* **70**, 174509 (2004).

Supporting Information

I Tunneling Spectroscopy

We have fabricated two devices that display distinct tunneling characteristics arising from variations in the tunneling interface during nanofabrication. Device 1 exhibits signatures of a soft superconducting gap, whereas device 2 shows signatures of a hard superconducting gap at $T = 50$ mK, as illustrated in Fig. S1.

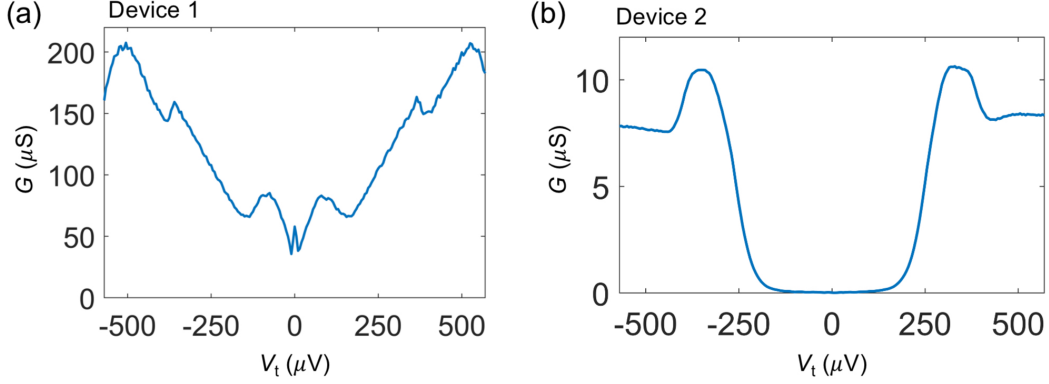


Figure S1: Tunneling gap. (a) Tunneling conductance G as a function of the bias voltage V_t in device 1. (b) Tunneling conductance G as a function of the bias voltage V_t for device 2.

II Tunneling conductance as a function of φ_L, φ_R for $V_t > \Delta$

Figures S2 and S3 show the tunneling conductance G as a function of independent phases φ_L and φ_R at fixed bias voltage V_t 's ($V_t > \Delta$) for devices 1 and 2, respectively. In device 1, the characteristic signature of the quartet-resonant family reappears at $V_t = 500$ μV , consistent with our observations at $V_t = 100$ μV in the main text. Similarly, in device 2, two families of quartet resonances emerge as the characteristic diamond-shaped pattern at $V_t = 350$ μV as shown in Fig. S3 (c).

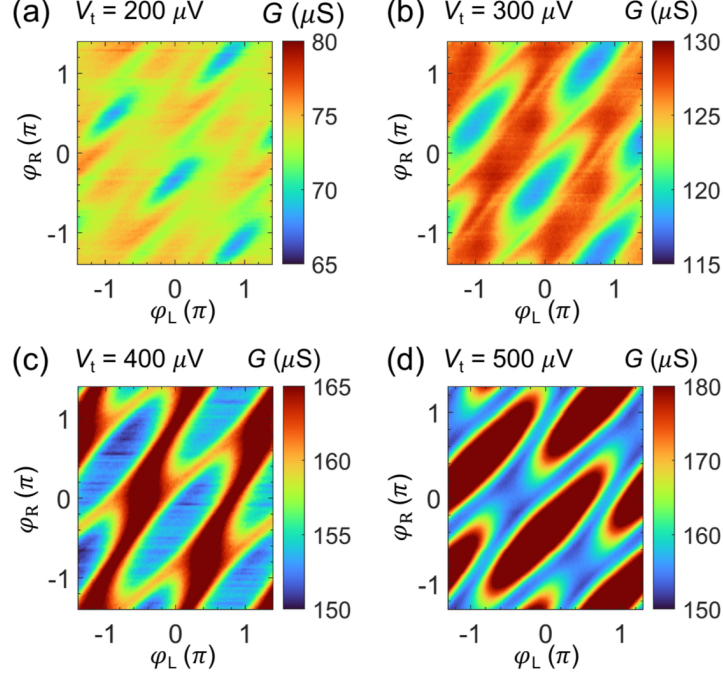


Figure S2: Tunneling spectroscopy in three-terminal JJ at $V_t \geq \Delta$. (a-d) Tunneling conductance G as a function of independent phases φ_L and φ_R governed by fluxes Φ_L and Φ_R at constant V_t 's ($V_t \geq \Delta$) for device 1. The colormaps are obtained by varying I_L and I_R with a step sized of $0.25 \mu\text{A}$ and $1 \mu\text{A}$ respectively. The colormaps are measured at $T = 200 \text{ mK}$ and back gate voltage $V_g = 0 \text{ V}$.

III Multipair Andreev resonances in 1D and 3D

In this section, we calculate the spectrum of resonances: the Cooper pairs and the Cooper quartets.

III.0.1 Cooper pair resonances

In this subsection, we calculate the spectrum of the Cooper-pair resonances. To describe proximity-induced Cooper-pair and multipair correlations in the graphene region, we employ the Dyson equation formalism, which provides a systematic framework to account for tunneling processes between the normal region and the superconducting leads to all orders. The general form of the Dyson equations is the following:

$$\hat{G}_{D,D} = \hat{g}_{D,D} + \hat{g}_{D,D} \hat{\Sigma}_{D,S} \hat{G}_{S,D}, \quad (1)$$

where \hat{G} and \hat{g} are the fully dressed and bare Nambu Green's function and $\hat{\Sigma}$ is the hopping self-energy. The subscript “D” refers to the “dot”, i.e. the piece of graphene, and the subscript “S” refers to the superconducting leads. The symbol “D” is used for a general rectangular-shaped 2D metal. Using:

$$\hat{G}_{S,D} = \hat{g}_{S,S} \hat{\Sigma}_{S,D} \hat{G}_{D,D} \quad (2)$$

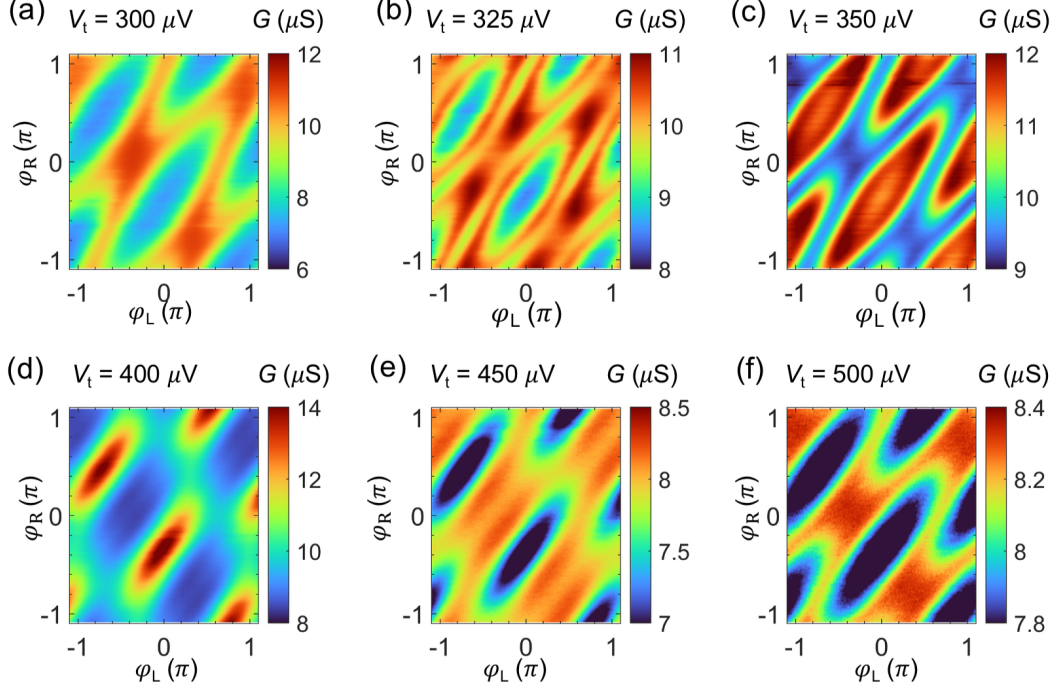


Figure S3: Tunneling spectroscopy for device 2 at $V_t \geq \Delta$. (a-f) Tunneling conductance G as a function of phases φ_L and φ_R at constant V_t 's ($V_t > \Delta$) for device 2. The colormaps are obtained by varying I_L and I_R with a step sized of $0.5 \mu\text{A}$ and $1 \mu\text{A}$, respectively. The colormaps are measured at $T = 50 \text{ mK}$ and back gate voltage $V_g = 0 \text{ V}$.

and combining Eqs. (1) with (2) lead to

$$\hat{G}_{D,D} = \hat{g}_{D,D} + \hat{g}_{D,D} \hat{\Sigma}_{D,S} \hat{g}_{S,S} \hat{\Sigma}_{S,D} \hat{G}_{D,D}, \quad (3)$$

This equation represents a closed system of linear equations for the fully dressed Nambu Green's function $\hat{G}_{D,D}$. At the next iteration, Eq. (3) can be rewritten as:

$$\hat{G}_{D,D} = \hat{g}_{D,D} + \hat{g}_{D,D} \hat{\Sigma}_{D,S} \hat{g}_{S,S} \hat{\Sigma}_{S,D} \hat{g}_{D,D} + \hat{g}_{D,D} \hat{\Sigma}_{D,S} \hat{g}_{S,S} \hat{\Sigma}_{S,D} \hat{g}_{D,D} \hat{\Sigma}_{D,S} \hat{g}_{S,S} \hat{\Sigma}_{S,D} \hat{G}_{D,D}. \quad (4)$$

Eqs. (3) and (4) are exact and are equivalent to each other.

We now apply an approximation in which the Green's functions are grouped pairwise, and the resulting set of paired Green functions is summed to infinite order in the form of a matrix geometric series. This random phase approximation (RPA) involves averaging, in real space, the modes (i.e. the pairs of Green's functions) over oscillations occurring on the scale of the Fermi wave-length λ_F , in a manner reminiscent of the formation of two-particle interference modes known as diffusons and Cooperons in disordered metals. In a ballistic 2D metal, the Cooper-pair modes are also known as *Andreev tubes*; see Refs. (5, 67). We denote the corresponding averaging by the double bracket $\langle\langle \dots \rangle\rangle$:

$$\langle\langle \hat{G}_{D,D} \rangle\rangle^{(pairs)} = \langle\langle \hat{g}_{D,D} \rangle\rangle + \langle\langle \hat{g}_{D,D} \hat{\Sigma}_{D,S} \hat{g}_{S,S} \hat{\Sigma}_{S,D} \hat{g}_{D,D} \rangle\rangle + \langle\langle \hat{g}_{D,D} \hat{\Sigma}_{D,S} \hat{g}_{S,S} \hat{\Sigma}_{S,D} \hat{g}_{D,D} \hat{\Sigma}_{D,S} \hat{g}_{S,S} \hat{\Sigma}_{S,D} \rangle\rangle \langle\langle \hat{G}_{D,D} \rangle\rangle^{(pairs)}, \quad (5)$$

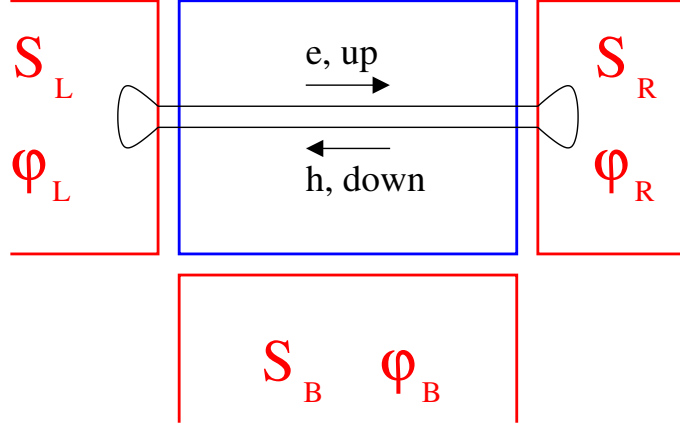


Figure S4: A diagram representing how a 1D Andreev tube propagating through the 2D metal connects two Andreev and inverse-Andreev reflection processes at the right and left superconductors S_R and S_L , respectively.

where we implement a kind of decoupling in the last term. Within this RPA, Eq. (5) is rewritten as

$$\langle\langle \hat{G}_{D,D} \rangle\rangle^{(pairs)} = [\hat{I} - \langle\langle \hat{g}_{D,D} \hat{\Gamma}_{D,D} \hat{g}_{D,D} \hat{\Gamma}_{D,D} \rangle\rangle]^{-1} \times [\langle\langle \hat{g}_{D,D} \rangle\rangle + \langle\langle \hat{g}_{D,D} \hat{\Gamma}_{D,D} \hat{g}_{D,D} \rangle\rangle], \quad (6)$$

where $\hat{\Gamma}_{D,D} = \hat{\Sigma}_{D,S} \hat{g}_{S,S} \hat{\Sigma}_{S,D}$, and $\langle\langle \hat{g}_{D,D} \rangle\rangle$ is local in space because it involves averaging over a single bare Green's function.

Next, we introduce the notations $\hat{g}_{D,D}^{loc}$ and $\hat{g}_{D,D}^{nonloc}$ for the local and the nonlocal Green's functions of the 2D metal, respectively. We also work within the phenomenological framework of the large-gap approximation (8, 68–71), which allows us to base the physical discussion on the simplest approximation. In this approximation, the normal bare Nambu-diagonal superconducting Green's functions $g_{S,S}^{1,1} = g_{S,S}^{2,2} = 0$ are taken to be vanishingly small. Under these conditions, Eq. (6) takes the following form:

$$\langle\langle \hat{G}_{D,D} \rangle\rangle^{(pairs)} = \hat{D}_0^{4 \times 4} [\langle\langle \hat{g}_{D,D} \rangle\rangle + \langle\langle \hat{g}_{D,D} \hat{\Gamma}_{D,D} \hat{g}_{D,D} \rangle\rangle], \quad (7)$$

where $\hat{D}_0^{4 \times 4}$ is expressed as a 4×4 matrix in the basis of the electron and hole Nambu labels, and the tight-binding sites α and β at both contacts:

$$\hat{D}_0^{4 \times 4} = \begin{pmatrix} 1 - \hat{K}_{D_\alpha, D_\alpha}^{1,1} & -\hat{K}_{D_\alpha, D_\beta}^{1,1} & -\hat{K}_{D_\alpha, D_\alpha}^{1,2} & -\hat{K}_{D_\alpha, D_\beta}^{1,2} \\ -\hat{K}_{D_\beta, D_\alpha}^{1,1} & 1 - \hat{K}_{D_\beta, D_\beta}^{1,1} & -\hat{K}_{D_\beta, D_\alpha}^{1,2} & -\hat{K}_{D_\beta, D_\beta}^{1,2} \\ -\hat{K}_{D_\alpha, D_\alpha}^{2,1} & -\hat{K}_{D_\alpha, D_\beta}^{2,1} & 1 - \hat{K}_{D_\alpha, D_\alpha}^{2,2} & -\hat{K}_{D_\alpha, D_\beta}^{2,2} \\ -\hat{K}_{D_\beta, D_\alpha}^{2,1} & -\hat{K}_{D_\beta, D_\beta}^{2,1} & -\hat{K}_{D_\beta, D_\alpha}^{2,2} & 1 - \hat{K}_{D_\beta, D_\beta}^{2,2} \end{pmatrix}, \quad (8)$$

where the kernel \hat{K} is:

$$\hat{K} = \hat{g}_{D,D} \hat{\Gamma}_{D,D} \hat{g}_{D,D} \hat{\Gamma}_{D,D}. \quad (9)$$

Each of the $\hat{\Gamma}$ matrices necessarily produces either an electron-hole Andreev reflection or a hole-electron inverse Andreev reflection within the large-gap approximation. The matrix \hat{K} contains a pair of $\hat{\Gamma}$ terms, and its off-diagonal Nambu elements are vanishingly small in this approximation, i.e. $\hat{K}^{1,2} = \hat{K}^{2,1} = 0$. Moreover, averaging over λ_F

causes products of local and nonlocal Green's functions to vanish, leading to a negligible contribution of $\langle\langle\hat{K}_{D_\alpha,D_\beta}\rangle\rangle$ for $\beta \neq \alpha$. A nonlocal component of the kernel \hat{K} is schematically illustrated in Fig. S4. We conclude that the matrix $\langle\langle\hat{D}_0^{4\times 4}\rangle\rangle$ becomes diagonal after averaging over rapid Fermi-phase oscillations on the scale of the Fermi wave-length λ_F , see the corresponding $\exp(\pm ik_F R_{\alpha,\beta})$ terms in the forthcoming Eqs. (15)-(18):

$$\langle\langle\hat{D}_0^{4\times 4}\rangle\rangle = \begin{pmatrix} 1 - \langle\langle\hat{K}_{D_\alpha,D_\alpha}^{1,1}\rangle\rangle & 0 & 0 & 0 \\ 0 & 1 - \langle\langle\hat{K}_{D_\beta,D_\beta}^{1,1}\rangle\rangle & 0 & 0 \\ 0 & 0 & 1 - \langle\langle\hat{K}_{D_\alpha,D_\alpha}^{2,2}\rangle\rangle & 0 \\ 0 & 0 & 0 & 1 - \langle\langle\hat{K}_{D_\beta,D_\beta}^{2,2}\rangle\rangle \end{pmatrix}. \quad (10)$$

Taking into account the first entry of Eq. (10), we find

$$1 - \langle\langle\hat{K}_{D_\alpha,D_\alpha}^{1,1}\rangle\rangle \simeq 1 - \hat{K}_{D_\alpha,D_\alpha}^{1,1,loc} - \langle\langle\hat{K}_{D_\alpha,D_\alpha}^{1,1,nonloc}\rangle\rangle, \quad (11)$$

with

$$\hat{K}_{D_\alpha,D_\alpha}^{1,1,loc} \simeq g_{\alpha,\alpha}^{1,1} \Gamma_{\alpha,\alpha}^{1,2} g_{\alpha,\alpha}^{2,2} \Gamma_{\alpha,\alpha}^{2,1} \quad (12)$$

$$\langle\langle\hat{K}_{D_\alpha,D_\alpha}^{1,1,nonloc}\rangle\rangle \simeq \langle\langle g_{\alpha,\beta}^{1,1} \Gamma_{\beta,\beta}^{1,2} g_{\beta,\alpha}^{2,2} \Gamma_{\alpha,\alpha}^{2,1}\rangle\rangle, \quad (13)$$

where $g_{\alpha,\alpha}^{1,1} = g_{\alpha,\alpha}^{2,2} \simeq i/W$, $\Gamma_{\alpha,\alpha}^{1,2} \simeq -(\Sigma_{D_\alpha,S_\alpha}^2/W) \exp(i\varphi_\alpha)$, $\Gamma_{\alpha,\alpha}^{2,1} \simeq -(\Sigma_{D_\alpha,S_\alpha}^2/W) \exp(-i\varphi_\alpha)$, and W is the largest energy scale set by the bandwidth of the normal region dispersion relation. We conclude that $\hat{K}_{D_\alpha,D_\alpha}^{1,1,loc} \simeq -\Sigma_{D_\alpha,S_\alpha}^4/W^4$ has a vanishingly small imaginary part, a result that will be used in the following calculations.

The inverse of each diagonal matrix element of Eq. (10) generically takes the following form:

$$\frac{1}{1 - K} = \frac{1}{1 - K_{loc} - K_{nonloc}} = \frac{1}{1 - K_{loc}} \sum_{n=0}^{+\infty} p^n, \quad (14)$$

where n is an integer, $p = K_{nonloc}/(1 - K_{loc})$, and “loc” and “non loc” in the subscript refer to the local and nonlocal components of the matrix \hat{K} . Constructive interference is possible only in the presence of a vanishingly small dephasing in the variable p . This type of interference is reminiscent of the proximity effect at a normal metal-insulator-superconductor (*NIS*) interface in the presence of nonmagnetic impurities in the normal region *N* (72–74). In the proximity effect, disorder-induced localization leads to multiple backscattering events at the *NIS* interface and, at low energies, enables constructive interference between the corresponding semiclassical trajectories of Andreev pairs.

Now, we provide the expression of the nonlocal Green's functions \hat{g}_{nonloc} which will subsequently be inserted into Eq. (13) and Eq. (14). Following a standard procedure, these Green's functions are obtained by integrating over the wave-vector k , which is treated as a continuous variable. In one dimension (1D), this yields the following expression for the nonlocal Green's function:

$$g_{\alpha,\beta,1,1}^{1D} \simeq \frac{1}{W} \exp \left[-i \left(k_F + \frac{\omega}{v_F} \right) R_{\alpha,\beta} \right] \quad (15)$$

$$g_{\alpha,\beta,2,2}^{1D} \simeq -\frac{1}{W} \exp \left[i \left(k_F - \frac{\omega}{v_F} \right) R_{\alpha,\beta} \right], \quad (16)$$

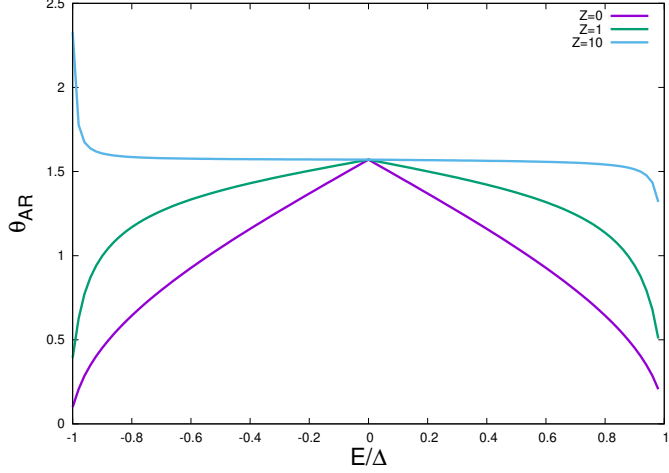


Figure S5: The phase shift θ_{AR} of a single Andreev reflection, calculated from Ref. (75), and plotted as a function of the energy E for the values $Z = 0, 1, 10$.

where $R_{\alpha,\beta}$ is the separation between the tight-binding sites α and β . In three dimensions (3D), we obtain a similar expression as Eqs. (15)-(16) in 1D, but with a geometrical prefactor:

$$g_{\alpha,\beta,1,1}^{3D} \simeq \frac{1}{Wk_F R_{\alpha,\beta}} \exp \left[-i \left(k_F + \frac{\omega}{v_F} \right) R_{\alpha,\beta} \right] \quad (17)$$

$$g_{\alpha,\beta,2,2}^{3D} \simeq -\frac{1}{Wk_F R_{\alpha,\beta}} \exp \left[i \left(k_F - \frac{\omega}{v_F} \right) R_{\alpha,\beta} \right]. \quad (18)$$

In Eqs. (17)-(18), we approximated the slowly-varying $(k_F \pm \omega/v_F)R_{\alpha,\beta}$ in the denominator of the geometrical prefactor by $k_F R_{\alpha,\beta}$.

By combining these orbital phase variables with the superconducting phases associated with electron-hole Andreev or hole-electron inverse-Andreev conversions in the superconductors, we find the following condition for full constructive interference:

$$\frac{2\omega R_{\alpha,\beta}}{\hbar v_F} \pm \varphi_L \mp \varphi_R + \pi = 2\pi n, \quad (19)$$

where n is an integer. The π -shift in Eq. (19) originates from the minus signs in Eqs. (16) and (18), which are arising from the pair of Andreev reflections contained in \hat{K}_{nonloc} . Each of these reflections contributes a phase shift of $\pi/2$ when the energy is small compared to the superconducting gap (75). Therefore, resonances whose real parts coincide with the energies of the Kulik spectrum are generated (2–4):

$$E_n^{(pairs)} = \frac{\hbar v_F}{2R_{\alpha,\beta}} \left[2\pi \left(n + \frac{1}{2} \right) \mp \chi_p \right], \quad (20)$$

where $\chi_p = \varphi_L - \varphi_R$ is the phase difference between the superconducting leads. Fig. S5 shows the phase shift θ_{AR} of a single Andreev reflection process at an arbitrary energy E within the superconducting gap Δ , for Blonder–Tinkham–Klapwijk (BTK) parameter values $Z = 0, 1, 10$ (75). The parameter Z characterizes the strength of the repulsive interfacial scattering potential, with high and low interface transparencies corresponding to $Z \ll 1$ and $Z \gg 1$, respectively. The phase shift θ_{AR} is obtained from $\theta_{AR} = \arg(a)$, where the Andreev reflection amplitude is

given by Eq. (A11a) in Ref. (75)

$$a = \frac{u_0 v_0}{\gamma}, \quad (21)$$

The coherence factors are denoted by

$$u_0^2 = \frac{1}{2} \left[1 + \frac{\sqrt{E^2 - \Delta^2}}{E} \right]. \quad (22)$$

and $v_0^2 = 1 - u_0^2$. The BTK notation $\gamma = u_0^2 + (u_0^2 - v_0^2)Z^2$ was used in Eq. (21).

By combining the phase shift θ_{AR} associated with a single NIS interface with Eq. (20) for the spectrum of a two-terminal long SNS junction, we obtain the following phenomenological expression for the ABS spectrum:

$$E_n^{(pairs)} = \frac{\hbar v_F}{2R_{\alpha,\beta}} [2\pi n + 2\theta_{AR} \mp \chi_p]. \quad (23)$$

III.0.2 Cooper quartet resonances

We now calculate the spectrum of the Cooper quartet resonances by extending the approximations to higher-order processes. Specifically, we expand the Dyson Eq. (4) as follows:

$$\hat{G}_{D,D} = \hat{g}_{D,D} \quad (24)$$

$$+ \hat{g}_{D,D} \hat{\Gamma}_{D,D} \hat{g}_{D,D} \quad (25)$$

$$+ \hat{g}_{D,D} \hat{\Gamma}_{D,D} \hat{g}_{D,D} \hat{\Gamma}_{D,D} \hat{g}_{D,D} \quad (26)$$

$$+ \hat{g}_{D,D} \hat{\Gamma}_{D,D} \hat{g}_{D,D} \hat{\Gamma}_{D,D} \hat{g}_{D,D} \hat{\Gamma}_{D,D} \hat{g}_{D,D} \quad (27)$$

$$+ \hat{g}_{D,D} \hat{\Gamma}_{D,D} \hat{g}_{D,D} \hat{\Gamma}_{D,D} \hat{g}_{D,D} \hat{\Gamma}_{D,D} \hat{g}_{D,D} \hat{\Gamma}_{D,D} \hat{G}_{D,D}. \quad (28)$$

We next group the nonlocal Green's functions pairwise, as indicated by the notation $\langle\langle \dots \rangle\rangle$, and find

$$\begin{aligned} \langle\langle \hat{G}_{D,D} \rangle\rangle^{(quartets)} &= \left[\hat{I} - \langle\langle \hat{g}_{D,D} \hat{\Gamma}_{D,D} \hat{g}_{D,D} \hat{\Gamma}_{D,D} \hat{g}_{D,D} \hat{\Gamma}_{D,D} \hat{g}_{D,D} \hat{\Gamma}_{D,D} \rangle\rangle \right]^{-1} \\ &\times \left[\langle\langle \hat{g}_{D,D} \rangle\rangle + \langle\langle \hat{g}_{D,D} \hat{\Gamma}_{D,D} \hat{g}_{D,D} \rangle\rangle \right. \\ &\quad \left. + \langle\langle \hat{g}_{D,D} \hat{\Gamma}_{D,D} \hat{g}_{D,D} \hat{\Gamma}_{D,D} \hat{g}_{D,D} \rangle\rangle \right. \\ &\quad \left. + \langle\langle \hat{g}_{D,D} \hat{\Gamma}_{D,D} \hat{g}_{D,D} \hat{\Gamma}_{D,D} \hat{g}_{D,D} \hat{\Gamma}_{D,D} \hat{g}_{D,D} \rangle\rangle \right]. \end{aligned} \quad (29)$$

We then phenomenologically decompose $L = \langle\langle \hat{g}_{D,D} \hat{\Gamma}_{D,D} \hat{g}_{D,D} \hat{\Gamma}_{D,D} \hat{g}_{D,D} \hat{\Gamma}_{D,D} \hat{g}_{D,D} \hat{\Gamma}_{D,D} \rangle\rangle$ into two terms q and L_1 . The former couples to the Cooper-quartet phase, while the latter do not:

$$q = \langle\langle \hat{g}_{\alpha,\beta}^{1,1} \hat{\Gamma}_{\beta,\beta}^{1,2} \hat{g}_{\beta,\gamma}^{2,2} \hat{\Gamma}_{\gamma,\gamma}^{2,1} \hat{g}_{\gamma,\beta}^{1,1} \hat{\Gamma}_{\beta,\beta}^{1,2} \hat{g}_{\beta,\alpha}^{2,2} \hat{\Gamma}_{\alpha,\alpha} \rangle\rangle \quad (30)$$

$$L_1 = \text{Sum of all remaining contractions}, \quad (31)$$

where the tight-binding sites α , β , and γ are the normal-metal counterparts of a , b , and c on the superconducting sides of the interfaces between N and S_a , S_b and S_c . The symbols a , b , and c are used as a generic labels for the superconductors and take values corresponding to all permutations of $\{S_L, S_R, S_B\}$.

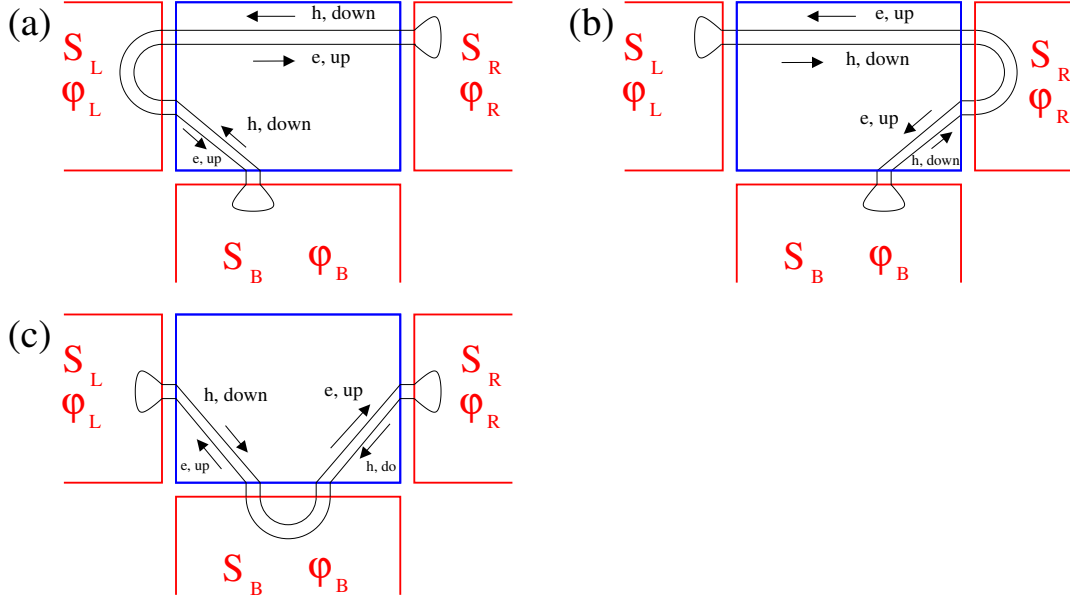


Figure S6: Copper quartet diagrams for 3TJJ. (a-c) The three lowest-order Cooper quartet diagrams, corresponding to the Q_L (a), Q_R (b), and Q_B (c) quartets. Those three types of Cooper quartets have the following Cooper quartet phase variables: $2\varphi_L - \varphi_R - \varphi_B$, $-\varphi_L + 2\varphi_R - \varphi_B$ and $-\varphi_L - \varphi_R + 2\varphi_B$, respectively. The resonance lines in the experiment are interpreted as arising from Q_L and Q_R in panels (a) and (b), respectively.

Figure S6 schematically shows the lowest order Cooper quartet diagrams contributing to q ; see Eq. (30). Panels (a), (b), and (c) of Fig. S6 show the three types of Cooper quartets that appear at lowest order in tunneling: the Q_L , Q_R and Q_B quartets, which transfer a charge $4e$ into S_L , S_R , and S_B , respectively.

The remaining terms L_1 in Eq. (31) include contributions that are insensitive to the superconducting phase variables. Other contributions within L_1 depend on second harmonics of the “local” Josephson relations, such as $2(\varphi_L - \varphi_R)$. We find

$$\frac{1}{1 - q - L_1} = \sum_{n_1, n_2} \frac{(n_1 + n_2)!}{n_1! n_2!} q^{n_1} L_1^{n_2}, \quad (32)$$

where n_1 and n_2 two integers. We impose the condition of full constructive interference by summing the simplest subseries with $n_2 = 0$. From this, we deduce the following Cooper-quartet resonance energies:

$$E_n^{(quartets)} = \frac{\hbar v_F}{2(R_{\alpha,\beta} + R_{\beta,\gamma})} [2\pi n \mp \chi_q], \quad (33)$$

where $\chi_q = \varphi_a + \varphi_b - 2\varphi_c$ is one of the Cooper-quartet phase variables associated with the superconductors S_a , S_b , and S_c . The superconducting leads S_a , S_b , and S_c with phases φ_a , φ_b and φ_c can take all permutations of the set $\{S_L, S_R, S_B\}$.

The Cooper-quartet spectrum in Eq. (33) is not shifted by a half-period because the four constituent Andreev reflections produce, at zero energy, a total phase shift of $4 \times (\pi/2) = 2\pi$, which is equivalent to zero modulo 2π .

We introduce the general phase shift $4\theta_{AR}$ associated with the four Andreev reflections, leading to the following

phenomenological expression for the Cooper-quartet spectrum:

$$E_n^{(quartets)} = \frac{\hbar v_F}{2(R_{\alpha,\beta} + R_{\beta,\gamma})} [2\pi n + 4\theta_{AR} \mp \chi_q]. \quad (34)$$

IV Tunneling spectroscopy

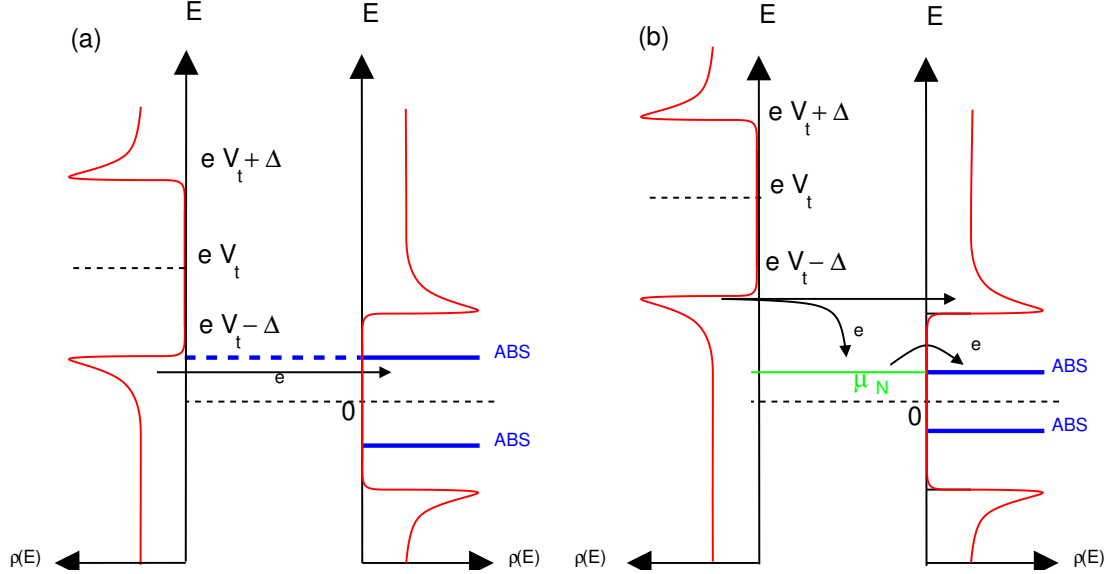


Figure S7: Energy as a function of density of states. The two spectroscopic modes: $V_t \leq 2\Delta$ (a) and $V_t \geq 2\Delta$ (b). The tunnel probe S_t is biased at the voltage V_t . Density of states are shown for the left, right and bottom grounded superconducting leads $\{S_L, S_R, S_B\}$ in each panel.

Here, we discuss how superconducting tunneling spectroscopy is implemented by a superconducting tunneling probe S_t , biased at voltage V_t , to the 2D metal, in the presence of three superconducting contacts $\{S_L, S_R, S_B\}$ forming a three-terminal Josephson junction. Using the Keldysh formalism, we recalculate the conductance in the Giaver regime (57), and establish a direct connection with our experimental observation.

We first consider a weak hopping amplitude $\Sigma_{a,\alpha} = \Sigma_{\alpha,a} \equiv \Sigma_a$ between the two superconductors S_a and S_α , and evaluate the current to the order $(\Sigma_a)^2$ in the presence of a bias voltage V . The “1,1” electron-electron Nambu component of the spectral current is given by

$$I_{1,1}(\omega) = \Sigma_{a,\alpha}^{1,1} (\hat{g}_{a,\alpha} \Sigma_{\alpha,a} \hat{g}_{a,a})^{+,-,1,1}(\omega, \omega) - \Sigma_{\alpha,a}^{1,1} (\hat{g}_{a,a} \hat{\Sigma}_{a,\alpha} \hat{g}_{\alpha,\alpha})^{+,-,1,1}(\omega, \omega), \quad (35)$$

where the superscripts “+,” “-” denote the Keldysh Green’s functions (76–78). In Eq. (35), the spectral current is diagonal both in the “1,1” electron-electron Nambu indices and in the frequency ω . We find

$$I_{1,1}(\omega) = \hat{\Sigma}_{a,\alpha}^{1,1} \hat{g}_{\alpha,\alpha}^{+,-,1,1}(\omega + eV) \hat{\Sigma}_{\alpha,a}^{1,1} \hat{g}_{a,a}^{A,1,1}(\omega) + \hat{\Sigma}_{a,\alpha}^{1,1} \hat{g}_{\alpha,\alpha}^{R,1,1}(\omega + eV) \hat{\Sigma}_{\alpha,a}^{1,1} \hat{g}_{a,a}^{+,-,1,1}(\omega) \quad (36)$$

$$- \hat{\Sigma}_{\alpha,a}^{1,1} \hat{g}_{a,a}^{+,-,1,1}(\omega - eV) \hat{\Sigma}_{a,\alpha}^{1,1} \hat{g}_{\alpha,\alpha}^{A,1,1}(\omega) - \hat{\Sigma}_{\alpha,a}^{1,1} \hat{g}_{a,a}^{R,1,1}(\omega - eV) \hat{\Sigma}_{a,\alpha}^{1,1} \hat{g}_{\alpha,\alpha}^{+,-,1,1}(\omega). \quad (37)$$

Additionally, taking into account the spectral current in the “2,2” hole-hole channel leads to the following expression for the current as a function of the bias voltage V :

$$I(V) = \int I(\omega)d\omega = 8\pi^2 (\Sigma_a)^2 \int d\omega \rho_{\alpha,\alpha}(\omega) \rho_{a,a}(\omega - eV) [n_F(\omega - eV) - n_F(\omega)], \quad (38)$$

where the spectral current is $I(\omega) = I_{1,1}(\omega) - I_{2,2}(\omega)$, and $\rho_{a,a}(\omega)$ and $\rho_{\alpha,\alpha}(\omega)$ denote the spectral densities of states of S_a and S_α , respectively. Reversing the signs of both the bias voltage V and the frequency ω in Eq. (38) yields $I(-V) = -I(V)$. The local density of states $\rho(\omega)$ of each BCS superconductor is proportional to the imaginary part of the bare Green’s function in the electron-electron channel: $\rho(\omega) = \text{Im}[g^A(\omega)]/\pi$, where $g^A(\omega) = -(\omega - i\eta)/W\sqrt{|\Delta|^2 - (\omega - i\eta)^2}$.

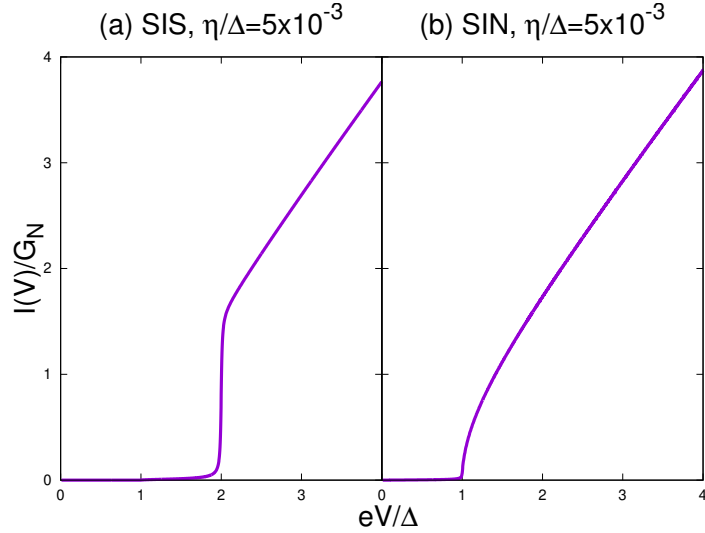


Figure S8: The current-voltage characteristics. (a-b) The current-voltage characteristics of a superconductor-superconductor weak link (a) and a superconductor-normal metal weak link (b). The voltage V is normalized to the superconducting gap Δ and the current I is normalized to the normal-state conductance G_N . The ratio between the Dynes parameter η and the superconducting gap Δ is $\eta/\Delta = 5 \times 10^{-3}$ on each panel.

Figure S8 shows the current-voltage characteristics derived from Eq. (38), for Giaver tunneling in both a *SIS* weak link [Fig. S8(a)] and a *SIN* weak link [see Fig. S8(b)].

We find that biasing a SIS tunnel junction at voltages $|eV_t| < 2\Delta$ results in the absence of tunneling current between the tunneling probe and any other superconducting terminal.

V Cooper quartet resonances in 2D

We now focus specifically on ABS for a 2D normal metal, in contrast to the 1D and 3D cases discussed earlier. Solutions of the wave equation in even dimensions exhibit a *wake* effect that is absent in odd dimension. We show that this wake effect has important consequences for the dependence of the tunneling spectra on the value of the bias voltage V_t applied to the tunneling probe.

Specifically, we obtain the following expressions for the nonlocal Green's function in 2D:

$$g_{\alpha,\beta,1,1}^{2D} \simeq \frac{i}{W\sqrt{k_F R}} \cos \left[\left(k_F + \frac{\omega}{v_F} \right) R - \frac{\pi}{4} \right] \quad (39)$$

$$g_{\alpha,\beta,2,2}^{2D} \simeq \frac{i}{W\sqrt{k_F R}} \cos \left[\left(k_F - \frac{\omega}{v_F} \right) R - \frac{\pi}{4} \right]. \quad (40)$$

These expressions contrast with the 1D and 3D counterparts given in Eqs. (15)-(16) and Eqs. (17)-(18), respectively. We next substitute Eqs. (39)-(40) into the kernel of Eq. (9) and note that the product $g_{\alpha,\beta,1,1}^{2D} g_{\alpha,\beta,2,2}^{2D}$ is real-valued. In 2D, the condition for full constructive interference therefore becomes equivalent to fixing the phase: $\chi_p = \varphi_R - \varphi_L = 2\theta_{AR} + 2\pi n$, where n is an integer, and θ_{AR} is defined in Eq. (23).

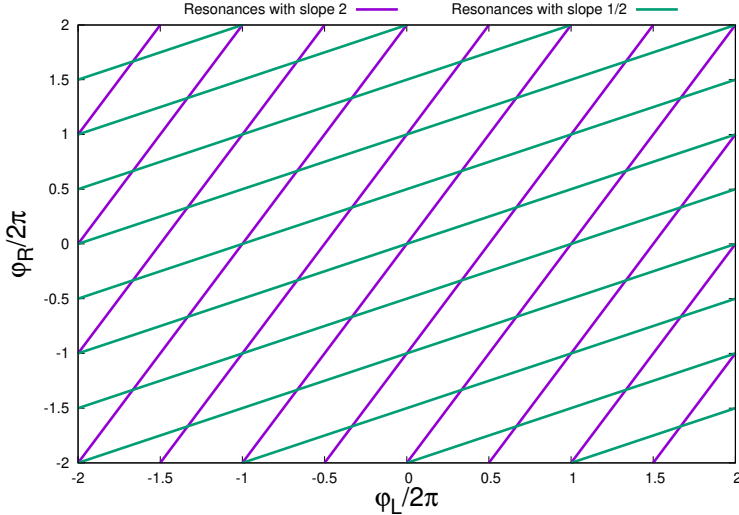


Figure S9: The two families of the Cooper quartet resonances: The resonances with slope 2 in the (φ_L, φ_R) diagram, and the resonances with slope 1/2, as defined in Eqs. (43) and (44).

A generalization to the Cooper quartets leads to $\chi_q = 4\theta_{AR} + 2\pi n$. The resulting Cooper quartet resonance lines are given by:

$$2\varphi_L - \varphi_R = 4\theta_{AR} + 2\pi n \quad (41)$$

$$-\varphi_L + 2\varphi_R = 4\theta_{AR} + 2\pi m, \quad (42)$$

These two relationships correspond to resonance lines with slopes 1/2 and 2 in the (φ_L, φ_R) plane of the superconducting phase differences, respectively. Here, we set $\varphi_B = 0$, as the phase reference. These equations can also be rearranged as follows:

$$\varphi_R = 2\varphi_L - 4\theta_{AR} - 2\pi n \quad (43)$$

$$\varphi_R = \frac{1}{2}\varphi_L + 2\theta_{AR} + \pi m. \quad (44)$$

We note that Eqs. (43)-(44) hold for all energies.

The above Eqs. (43)-(44) are schematically illustrated in Fig. S9, highlighting the two families of Cooper-quartet resonances. Within this simple model, the two families intersect freely without hybridization. By contrast, the experimental data reveal avoided crossings, indicating hybridization between the corresponding quartet modes.

VI Theoretical Cooper-quartet diagram

We begin by evaluating the Cooper-quartet diagram shown in Fig. S6 (a). The spectral current transmitted from the 2D metal N to the superconductor S_R takes the following form:

$$I_R(\omega) = \text{Nambu-trace} \left\{ \hat{\sigma}_z \left[\hat{\Sigma}_{R,r} \hat{G}_{r,R}^{+,-} - \hat{\Sigma}_{r,R} \hat{G}_{R,r}^{+,-} \right] \right\}. \quad (45)$$

Expanding this equation, we find (79)

$$\frac{\partial I_R}{\partial \mu_N} \approx \frac{\gamma_R \gamma_L^2 \gamma_B}{W^4} \frac{1}{(k_F R_{r,l})(k_F R_{l,b})} \cos \left(\frac{2\mu_N R_{r,l}}{\hbar v_F} \right) \cos \left(\frac{2\mu_N R_{l,b}}{\hbar v_F} \right) \cos (2\varphi_L - \varphi_R - \varphi_B). \quad (46)$$

Here, we have discarded a prefactor of order unity and chosen the superconducting phase variables such that Eq. (43) is satisfied, i.e., $2\varphi_L - \varphi_R - \varphi_B = 4\theta_{AR} + 2\pi n$ in Fig. S6 (a). The labels R , L , and B stand for the tight-binding sites supporting the Cooper quartet resonances in the superconducting leads, while their counterparts in the normal metal N are denoted by r , l , and b , respectively. We also note that current conservation relates the tunneling conductance to the Cooper-quartet current: the condition $I_t + I_R + I_L + I_B = 0$ implies $\partial I_t / \partial \mu_N = -\partial (I_R + I_L + I_B) / \partial \mu_N$.

We now assume that the dominant contribution to the current arises from the (l, b) section of the quartet diagram that is located near the bottom-left corner of the normal-metal N ; see Fig. S6 (a). This assumption maximizes the product of the geometrical prefactors $1/(k_F R_{r,l})(k_F R_{l,b})$. Therefore, we find

$$-\frac{\partial I_R}{\partial \mu_N} \approx -\frac{\gamma_R \gamma_L^2 \gamma_B}{W^4} \frac{1}{(k_F R_{r,l})} \cos \left(\frac{2\mu_N R_{r,l}}{\hbar v_F} \right) \cos (2\varphi_L - \varphi_R - \varphi_B), \quad (47)$$

where we implemented $R_{l,b} = 0$ in the $\cos(2\mu_N R_{l,b}/\hbar v_F)$ term of Eq. (46) and, taking the local limit of the (l, b) contact in the geometrical prefactor, we replaced $k_F R_{l,b}$ by unity. We conclude the following phenomenological expression of the dimensionless conductance:

$$g_0(\varphi_L, \varphi_R, V_{t,eff}) = -\cos(\alpha \mu_{N,eff}^*(V_{t,eff})) \delta_{eff} (2\varphi_L - \varphi_R - 4\theta_{AR}) - \cos(\alpha \mu_{N,eff}^*(V_{t,eff})) \delta_{eff} (2\varphi_R - \varphi_L - 4\theta_{AR}), \quad (48)$$

where we have included both types of Cooper-quartet resonances (Eqs. (43)-(44)) and phenomenologically introduced the nonequilibrium electrochemical potential $\mu_{N,eff}^*(V_{t,eff}) = \sqrt{V_{t,eff}^2 - (2\Delta)^2}$. The notation δ_{eff} in Eq. (48) denotes a δ -function broadened by a Lorentzian along both the φ_R - and the φ_L -axes:

$$g_0(\varphi_L, \varphi_R, V_{t,eff}) = -\cos(\alpha \mu_{N,eff}^*(V_{t,eff})) \int \frac{dt}{\pi^2} \frac{\eta_0}{[(\varphi_R - \varphi_{R,1}(t))^2 + \eta_0^2]} \frac{\eta_0}{[(\varphi_L - \varphi_{L,1}(t))^2 + \eta_0^2]} \quad (49)$$

$$-\cos(\alpha \mu_{N,eff}^*(V_{t,eff})) \int \frac{dt}{\pi^2} \frac{\eta_0}{[(\varphi_R - \varphi_{R,2}(t))^2 + \eta_0^2]} \frac{\eta_0}{[(\varphi_L - \varphi_{L,2}(t))^2 + \eta_0^2]}, \quad (50)$$

where $2\varphi_{L,1}(t) - \varphi_{R,1}(t) = 4\theta_{AR}$ and $\varphi_{L,2}(t) - 2\varphi_{R,2}(t) = 4\theta_{AR}$ for both Cooper quartet resonance lines in Eqs. (44) and (43), respectively, i.e.

$$\varphi_{L,1}(t) = \frac{t}{2} \quad (51)$$

$$\varphi_{R,1}(t) = t + 4\theta_{AR} \quad (52)$$

and

$$\varphi_{L,2}(t) = t + 4\theta_{AR} \quad (53)$$

$$\varphi_{R,2}(t) = \frac{t}{2}. \quad (54)$$

Fig. S10 shows the resulting conductance maps for a selection of the dimensionless voltages $V_{t,eff}$. We conclude that the model is qualitatively compatible with the main features of the experiment.

VII Robustness of the Cooper quartet resonances

VII.0.1 Robustness with respect to weak disorder

In this subsubsection, we argue that the Cooper quartet resonances are immune with respect to weak disorder. Coming back to a long two-terminal *SNS* Josephson junction, we note that different situations can be met upon increasing the amount of disorder. Fig. S11 (a) shows the Andreev tubes in a clean *SNS* device. Those tubes are parallel to the x -axis, due to the conserved quantum numbers of the transverse modes forming standing wave in the considered perfect wave-guide geometry. The experimental devices of the paper are as clean as possible, due to the encapsulation of the graphene layer by two hBN layers on top and bottom, and to the contacts at the edges. Small residual disorder can distort the Andreev tubes as shown in Fig. S11 (b). On this figure, the elastic mean free path is large and summing over all of the transverse channels yields the oscillating factors in the transmission modes deduced from Eqs. (39)-(40):

$$T \sim \frac{1}{\delta l} \int_{l_0-\delta l/2}^{l_0+\delta l/2} dl \cos \left[\left(k_F + \frac{\omega}{v_F} \right) l - \frac{\pi}{4} \right] \cos \left[\left(k_F - \frac{\omega}{v_F} \right) l - \frac{\pi}{4} \right]. \quad (55)$$

It is deduced that all Andreev tubes keep their coherence upon including a distribution $\mathcal{P}(l)$ of the tube length l , characterized by the root-mean-square δl such that $2\omega\delta l/\hbar v_F \lesssim 1$, see Fig. S11 (b). As the level of disorder is increased, the typical semiclassical trajectories start to scatter between the nonmagnetic impurities, see Fig. S11 (c). The semiclassical trajectories connecting the left to the right side of the normal metal N are characterized by the root-mean-square $\delta l \gg \hbar v_F/2\omega$ in their distribution. As a result of the corresponding destructive interference, the energy oscillations of the supercurrent are damped by a strongly decaying exponential envelope above the Thouless energy (80–92). This contrasts with the coherent oscillations in the clean limit (38, 39).

VII.0.2 Robustness with respect to scattering Cooper pairs at the 2D metal-*S* boundaries

We note that scattering Andreev tubes at the open boundary of the 2D metal, see Fig. S12 (a), can change the magnetic field dependence of the corresponding Fraunhofer pattern, see Ref. (67). In this subsection, we demonstrate that

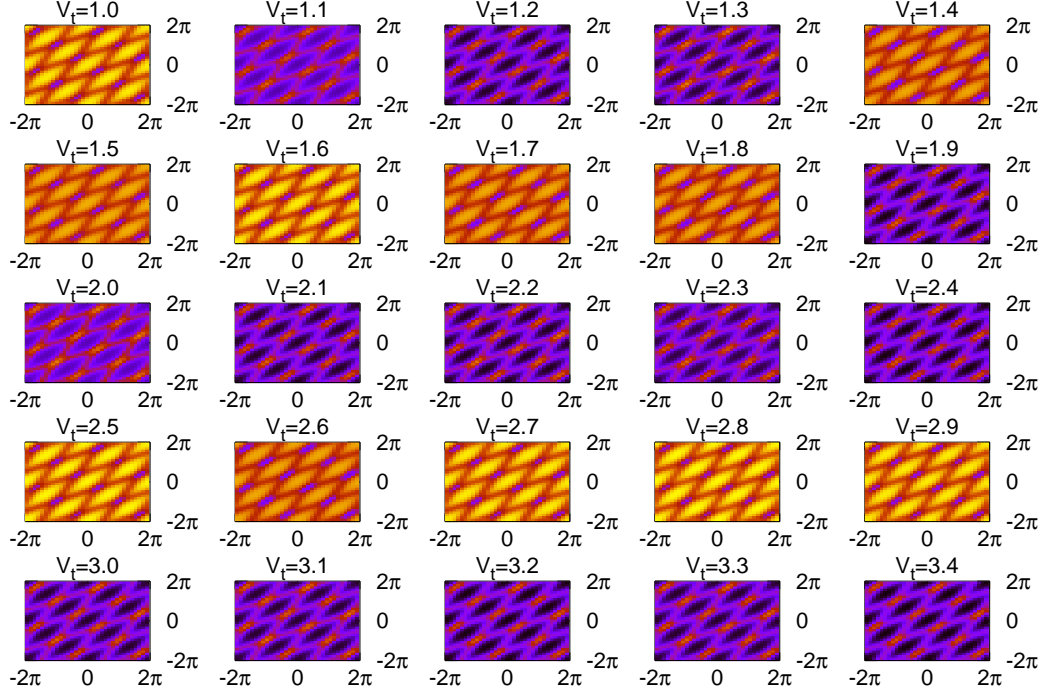


Figure S10: Theoretically calculated tunneling conductance maps. Calculated tunneling conductance in the plane of the two phase variables (φ_L, φ_R) , for the different values of dimensionless $V_{t,eff}$. The value $V_{t,eff} = 1$ corresponds to bias voltage equal to twice the superconducting gap. We find evidence for the two families of resonances. As a result of the 2D quantum wake effect, the location of the resonances does not move as a function of $V_{t,eff}$ in the (φ_L, φ_R) plane, only their sign oscillates between negative and positive values.

scattering Andreev tubes at the 2D metal-superconductor interfaces, see Fig. S12 (b), does not contribute to the current. Conversely, scattering Andreev tubes at a 2D metal-normal metal interface, see Fig. S12 (c), contributes for a finite value to the current.

We start with evaluating the current associated to Andreev tubes propagating between the interfaces with the left and right superconductors S_L and S_R , and bouncing once on the interface between the 2D metal and the bottom superconductor S_B , see the diagram in Fig. S12 (b). The current I_L transmitted at the left contact with S_L is expressed in terms of the fully dressed Nambu Green's function $\hat{G}^{+,-}$, see Refs. (76–78):

$$I_L = \text{Nambu trace} \left\{ \hat{\tau}_3 \left[\hat{\Sigma}_{\alpha,a} \hat{G}_{a,\alpha}^{+,-} - \hat{\Sigma}_{a,\alpha} \hat{G}_{\alpha,a}^{+,-} \right] \right\}. \quad (56)$$

Assuming a large superconducting gap and a continuous 2D metal density of states leads to a finite value for the

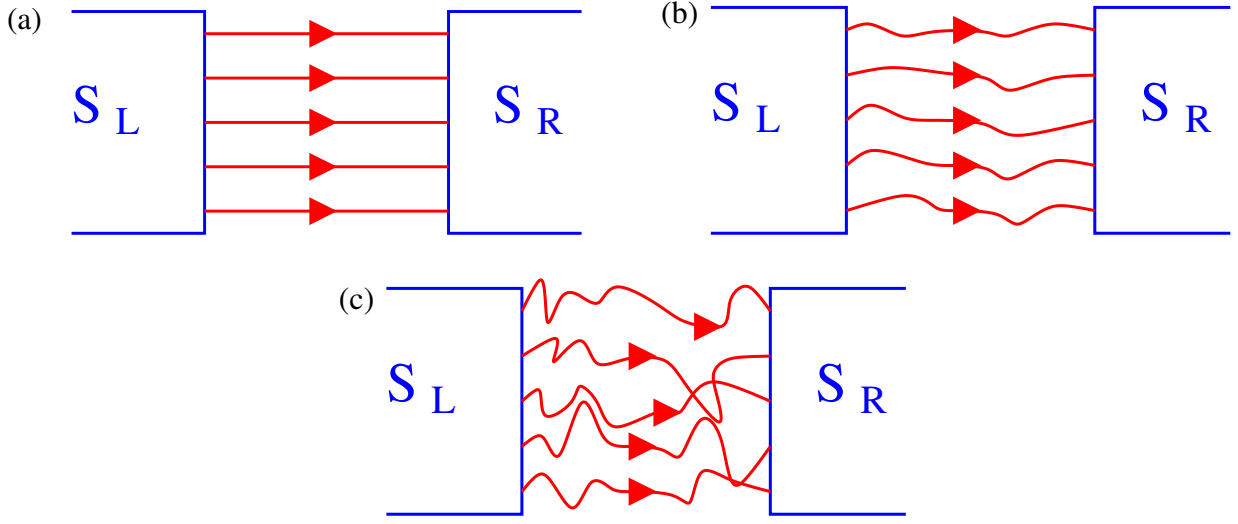


Figure S11: Andreev tubes. Typical shape of the Andreev tubes: (a) in the absence of disorder, (b) with weak disorder, and (c) in the diffusive limit.

corresponding Keldysh Green's function, which leads to the following expression of $\hat{G}_{a,a}^{+,-}$:

$$\hat{G}_{a,a}^{+,-} = \hat{g}_{a,a}^R \hat{\Sigma}_{a,a} \hat{g}_{\alpha,\beta}^{+,-} \hat{\Sigma}_{\beta,b} \hat{g}_{b,c}^A \hat{\Sigma}_{c,\gamma} \hat{g}_{\gamma,\delta}^A \hat{\Sigma}_{\delta,d} \hat{g}_{d,d}^A \hat{\Sigma}_{d,\delta} \hat{g}_{\delta,\gamma}^A \hat{\Sigma}_{\gamma,c} \hat{g}_{c,b}^A \hat{\Sigma}_{b,\beta} \hat{g}_{\beta,\alpha}^A \quad (57)$$

$$+ \hat{g}_{a,a}^R \hat{\Sigma}_{a,a} \hat{g}_{\alpha,\beta}^R \hat{\Sigma}_{\beta,b} \hat{g}_{b,c}^R \hat{\Sigma}_{c,\gamma} \hat{g}_{\gamma,\delta}^{+,-} \hat{\Sigma}_{\delta,d} \hat{g}_{d,d}^A \hat{\Sigma}_{d,\delta} \hat{g}_{\delta,\gamma}^A \hat{\Sigma}_{\gamma,c} \hat{g}_{c,b}^A \hat{\Sigma}_{b,\beta} \hat{g}_{\beta,\alpha}^A \quad (58)$$

$$+ \hat{g}_{a,a}^R \hat{\Sigma}_{a,a} \hat{g}_{\alpha,\beta}^R \hat{\Sigma}_{\beta,b} \hat{g}_{b,c}^R \hat{\Sigma}_{c,\gamma} \hat{g}_{\gamma,\delta}^R \hat{\Sigma}_{\delta,d} \hat{g}_{d,d}^R \hat{\Sigma}_{d,\delta} \hat{g}_{\delta,\gamma}^{+,-} \hat{\Sigma}_{\gamma,c} \hat{g}_{c,b}^A \hat{\Sigma}_{b,\beta} \hat{g}_{\beta,\alpha}^A \quad (59)$$

$$+ \hat{g}_{a,a}^R \hat{\Sigma}_{a,a} \hat{g}_{\alpha,\beta}^R \hat{\Sigma}_{\beta,b} \hat{g}_{b,c}^R \hat{\Sigma}_{c,\gamma} \hat{g}_{\gamma,\delta}^R \hat{\Sigma}_{\delta,d} \hat{g}_{d,d}^R \hat{\Sigma}_{d,\delta} \hat{g}_{\delta,\gamma}^R \hat{\Sigma}_{\gamma,c} \hat{g}_{c,b}^R \hat{\Sigma}_{b,\beta} \hat{g}_{\beta,\alpha}^{+,-}. \quad (60)$$

Given the assumption of a large gap and the forms (39)-(40) of the 2D metal Green's functions, we obtain the following identities:

$$0 = \hat{g}_{\alpha,\beta}^{+,-} \hat{\Sigma}_{\beta,b} \hat{g}_{b,c}^A \hat{\Sigma}_{c,\gamma} \hat{g}_{\gamma,\delta}^A + \hat{g}_{\alpha,\beta}^R \hat{\Sigma}_{\beta,b} \hat{g}_{b,c}^R \hat{\Sigma}_{c,\gamma} \hat{g}_{\gamma,\delta}^{+,-} \quad (61)$$

$$0 = \hat{g}_{\delta,\gamma}^{+,-} \hat{\Sigma}_{\gamma,c} \hat{g}_{c,b}^A \hat{\Sigma}_{b,\beta} \hat{g}_{\beta,\alpha}^A + \hat{g}_{\delta,\gamma}^R \hat{\Sigma}_{\gamma,c} \hat{g}_{c,b}^R \hat{\Sigma}_{b,\beta} \hat{g}_{\beta,\alpha}^{+,-}, \quad (62)$$

from what we deduce that the corresponding current is vanishingly small: $I_L \equiv I_a = 0$ because $\hat{G}_{a,a}^{+,-} = 0$ and $\hat{G}_{a,a}^{+,-} = 0$ in Eq. (56). Identities similar to Eqs. (61)-(62) are also operational in elastic cotunneling (EC) at a normal metal-superconductor-normal metal double interface, evaluated at the lowest order in the tunneling amplitudes. In this case, it is known (93, 94) that, in linear response, the current is proportional to the difference between the right and left electrochemical potentials, which implies that the EC current is vanishingly small if both electrochemical potentials are identical, as it is the case in the processes of scattering Andreev tubes on a single interface.

We conclude that scattering Andreev tubes on the boundaries is not effective in all-superconducting devices. Consequently, the Andreev tubes are parallel to the x -axis in Andreev interferometers, which is compatible with the experimental robustness of the coherent ABS oscillations reported in Ref. (38), and, in the present paper, with the robustness of the quartet ABS oscillations as the voltage V_t is increased on the superconducting tunneling probe.

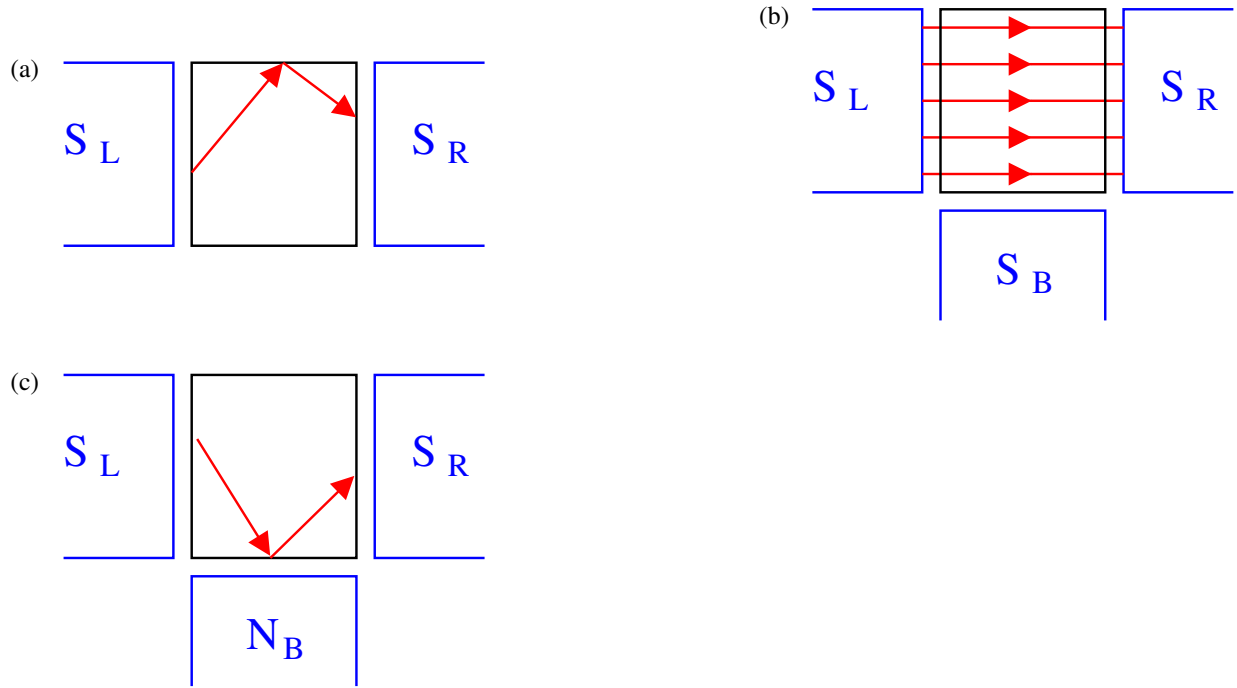


Figure S12: Reflection of the Andreev tubes at an open boundary. (a), absence of reflection at the boundary with the superconductor S_B (b) and reflection at the boundary with the normal metal N_B (c).

Conversely, the above argument can easily be generalized to scattering Andreev tubes at a 2D normal metal-3D metal interface, and a nonvanishingly small current is found in this case. The Andreev tube then scatter at the normal contact interface, in a way that is qualitatively similar to scattering on nonmagnetic impurities. The resulting destructive interference between tubes of different lengths is compatible with the absence of robustness of the coherent ABS oscillations as the voltage is increased on the normal contact of a *SSN* Andreev interferometer, see Ref. (38).